



A NEW POPULATION OF COMPTON-THICK AGNs IDENTIFIED USING THE SPECTRAL CURVATURE ABOVE 10 keV

MICHAEL J. KOSS^{1,2,18}, R. ASSEF³, M. BALOKOVIĆ⁴, D. STERN⁵, P. GANDHI⁶, I. LAMPERTI¹, D. M. ALEXANDER⁷,
D. R. BALLANTYNE⁸, F. E. BAUER^{9,10}, S. BERNEY¹, W. N. BRANDT^{11,12,13}, A. COMASTRI¹⁴, N. GEHRELS¹⁵, F. A. HARRISON⁴,
G. LANSBURY⁷, C. MARKWARDT¹⁵, C. RICCI⁹, E. RIVERS⁴, K. SCHAWINSKI¹, B. TRAKHTENBROT¹, E. TREISTER¹⁶, AND
C. MEGAN URRY¹⁷

¹ Institute for Astronomy, Department of Physics, ETH Zurich, Wolfgang-Pauli-Strasse 27, CH-8093 Zurich, Switzerland; mkoss@phys.ethz.ch

² Institute for Astronomy, University of Hawaii, 2680 Woodlawn Drive, Honolulu, HI 96822, USA

³ Núcleo de Astronomía de la Facultad de Ingeniería, Universidad Diego Portales, Av. Ejército 441, Santiago, Chile

⁴ Cahill Center for Astronomy and Astrophysics, California Institute of Technology, Pasadena, CA 91125, USA

⁵ Jet Propulsion Laboratory, California Institute of Technology, Pasadena, CA 91109, USA

⁶ School of Physics and Astronomy, University of Southampton, Highfield, Southampton SO17 1BJ, UK

⁷ Department of Physics, Durham University, South Road, Durham DH1 3LE, UK

⁸ Center for Relativistic Astrophysics, School of Physics, Georgia Institute of Technology, Atlanta, GA 30332, USA

⁹ Instituto de Astrofísica, Facultad de Física, Pontificia Universidad Católica de Chile, Casilla 306, Santiago 22, Chile

¹⁰ Space Science Institute, 4750 Walnut Street, Suite 205, Boulder, CO 80301, USA

¹¹ Department of Astronomy & Astrophysics, 525 Davey Lab, The Pennsylvania State University, University Park, PA 16802, USA

¹² Institute for Gravitation and the Cosmos, The Pennsylvania State University, University Park, PA 16802, USA

¹³ Department of Physics, 104 Davey Lab, The Pennsylvania State University, University Park, PA 16802, USA

¹⁴ INAF—Osservatorio Astronomico di Bologna, Via Ranzani 1, I-40127 Bologna, Italy

¹⁵ Astrophysics Science Division, NASA Goddard Space Flight Center, Greenbelt, MD, USA

¹⁶ Departamento de Astronomía, Universidad de Concepción, Casilla 160-C, Concepción, Chile

¹⁷ Yale Center for Astronomy and Astrophysics, Physics Department, Yale University, P.O. Box 208120, New Haven, CT 06520-8120, USA

Received 2015 December 1; revised 2016 March 29; accepted 2016 April 18; published 2016 July 6

ABSTRACT

We present a new metric that uses the spectral curvature (SC) above 10 keV to identify Compton-thick active galactic nuclei (AGNs) in low-quality *Swift*/Burst Alert Telescope (BAT) X-ray data. Using *NuSTAR*, we observe nine high SC-selected AGNs. We find that high-sensitivity spectra show that the majority are Compton-thick (78% or 7/9) and the remaining two are nearly Compton-thick ($N_{\text{H}} \simeq (5-8) \times 10^{23} \text{ cm}^{-2}$). We find that the SC_{BAT} and $\text{SC}_{\text{NuSTAR}}$ measurements are consistent, suggesting that this technique can be applied to future telescopes. We tested the SC method on well-known Compton-thick AGNs and found that it is much more effective than broadband ratios (e.g., 100% using SC versus 20% using 8–24 keV/3–8 keV). Our results suggest that using the >10 keV emission may be the only way to identify this population since only two sources show Compton-thick levels of excess in the Balmer decrement corrected [O III] to observed X-ray emission ratio ($F_{[\text{O III}]}/F_{2-10 \text{ keV}}^{\text{obs}} > 1$) and *WISE* colors do not identify most of them as AGNs. Based on this small sample, we find that a higher fraction of these AGNs are in the final merger stage (<10 kpc) than typical BAT AGNs. Additionally, these nine obscured AGNs have, on average, $\approx 4\times$ higher accretion rates than other BAT-detected AGNs ($\langle \lambda_{\text{Edd}} \rangle = 0.068 \pm 0.023$ compared to $\langle \lambda_{\text{Edd}} \rangle = 0.016 \pm 0.004$). The robustness of SC at identifying Compton-thick AGNs implies that a higher fraction of nearby AGNs may be Compton-thick ($\approx 22\%$) and the sum of black hole growth in Compton-thick AGNs (Eddington ratio times population percentage) is nearly as large as mildly obscured and unobscured AGNs.

Key words: galaxies: active – galaxies: Seyfert – X-rays: galaxies

1. INTRODUCTION

While there has been great progress understanding the origin of the cosmic X-ray background (CXB) and the evolution of active galactic nuclei (AGNs) with *XMM-Newton* and *Chandra* (e.g., Brandt & Alexander 2015), it is clear that a significant fraction of the >8 keV background is not produced by known 2–8 keV sources (Worsley et al. 2005; Luo et al. 2011; Xue et al. 2012). This background probably originates from a high-column-density, low-redshift population ($z < 1$). However, the source of the bulk of the CXB’s surface brightness, peaking at ≈ 30 keV, is still unknown. The measurement of the space density and evolution of this population of highly absorbed AGNs, as well as the derivation of their column density distribution function with luminosity

and redshift, is crucial for understanding the cosmic growth of black holes. Population-synthesis models attempt to explain the CXB by introducing appropriate numbers of absorbed Seyferts (e.g., Treister & Urry 2005; Gilli et al. 2007). However, studies suggest that the number of Compton-thick AGNs ($N_{\text{H}} > 10^{24} \text{ cm}^{-2}$) is a factor of 3–4 smaller than expected in the population-synthesis models (e.g., Treister et al. 2009), at least in the local universe (Ajello et al. 2012). Additional studies suggest that Compton-thick AGNs evolve differently than other obscured sources and are more likely associated with rapid black hole growth at higher redshift (e.g., Draper & Ballantyne 2010; Treister et al. 2010). These problems limit our current knowledge of the origin of the CXB at >10 keV.

In many well-studied objects, obscuration significantly attenuates the soft X-ray, optical, and UV signatures of AGNs. There are only two spectral bands, the ultra-hard X-ray (>10 keV) and the mid-infrared (5–50 μm), where this

¹⁸ SNSF Ambizione Fellow.

obscuring material is optically thin up to high column densities $N_{\text{H}} < 10^{24} \text{ cm}^{-2}$ (Compton-thin). Thus, these spectral bands are optimal for less biased AGN searches (e.g., Treister et al. 2004; Stern et al. 2005; Alexander et al. 2008). Radio selection of AGNs is also largely obscuration independent, though only $\sim 10\%$ of AGNs are radio loud (e.g., Miller et al. 1990; Stern et al. 2000), and finding a radio excess in radio-quiet AGNs can be difficult because of the host galaxy contribution from star formation (Del Moro et al. 2013) and significant free-free absorption from the ionized torus (Roy et al. 2000). Mid-IR selection is very effective at identifying high-luminosity AGNs, where the nuclear emission dominates, but moderate-luminosity AGNs, like those common in the local universe, are harder to identify because the host galaxy contribution is relatively larger (e.g., Cardamone et al. 2008; Eckart et al. 2010; Donley et al. 2012; Stern et al. 2012). In contrast, X-ray surveys suffer little contamination from non-nuclear emission at typical survey depths, and thus a hard X-ray survey can efficiently find both low- and high-luminosity AGNs in a uniform fashion, including even the heavily obscured, lower-luminosity AGNs, which we expect to be important contributors to the CXB.

The Burst Alert Telescope (BAT; Barthelmy et al. 2005), a large field of view (1.4 sr) coded aperture imaging instrument on the *Swift* satellite, has surveyed the sky to unprecedented depth. The all-sky BAT survey is a factor of ≈ 20 more sensitive than previous satellites such as *HEAO 1* (Levine et al. 1984). BAT selection is particularly powerful because it uses the 14–195 keV band, which can pass through obscuring material of $N_{\text{H}} > 10^{24} \text{ cm}^{-2}$, though it is still biased against the most obscured AGNs (e.g., $> 10^{25} \text{ cm}^{-2}$; Lanzuisi et al. 2015a). It is therefore sensitive to most obscured AGNs where even moderately hard X-ray surveys ($\sim 10 \text{ keV}$) are severely reduced in sensitivity. The 70-month *Swift*/BAT survey has identified 1210 objects, of which 823 are AGNs, while the rest are overwhelmingly Galactic in origin (Baumgartner et al. 2013). Higher angular resolution X-ray data for every source were obtained with the *Swift* X-ray Telescope (Burrows et al. 2005) because of the large positional uncertainty of *Swift*/BAT ($\approx 6'$) for fainter sources.

Unfortunately, due to the large number of sources spread across the sky and the limited sensitivity of *Swift*/XRT to obscured sources, X-ray follow-up and identification of the entire BAT catalog of ≈ 800 AGNs have been difficult. Survey programs typically used the first year or two of stacked data (e.g., 9-month Survey, PI R. Mushotzky; Northern Galactic Cap 22-month Survey, PI N. Brandt). After 10 yr of the mission, one can detect many more obscured AGNs, which are critical to estimating the fraction of Compton-thick AGNs and the source of the CXB. Additionally, the majority of sources had *Swift*/XRT coverage, which is insufficient for measuring the column density (N_{H}) in heavily obscured AGNs (Winter et al. 2009). Finally, accurately estimating column densities based on *Swift*/XRT and BAT data is problematic because of time variability and the low signal-to-noise ratio of typical BAT detections (Vasudevan et al. 2013).

To make progress in this area requires (1) an ultra-hard X-ray survey of sufficient sensitivity, angular resolution, and solid angle coverage at $\approx 30 \text{ keV}$ to identify a large number of sources and (2) high-sensitivity observations to obtain the column density of the sources, their detailed X-ray spectral properties, and confirmations of their identifications. With the new focusing optics on the *Nuclear Spectroscopic Telescope*

Array (*NuSTAR*; Harrison et al. 2013), the entire 3–79 keV energy range can be studied at sensitivities more than $100\times$ better than those of previous coded aperture mask telescopes such as *Swift*/BAT or *INTEGRAL*. This enables detailed X-ray modeling of heavily obscured AGNs (e.g., Arévalo et al. 2014; Baloković et al. 2014; Bauer et al. 2014; Gandhi et al. 2014; Puccetti et al. 2014; Brightman et al. 2015; Koss et al. 2015).

In this article, we combine the all-sky nature of *Swift*/BAT with the unprecedented *NuSTAR* sensitivity over a wide energy range to develop a new technique to find previously unknown heavily obscured AGNs. The 10–100 keV spectrum becomes increasingly curved with increasing absorption. This is especially useful in selecting Compton-thick AGNs because of its effectiveness up to very high column densities ($N_{\text{H}} \sim 10^{25} \text{ cm}^{-2}$). Additionally, detection based solely on spectral curvature (SC) offers an important test of AGN torus models and is less biased against Compton-thick AGNs. In Section 2, we detail the *NuSTAR* sample and the SC selection. Section 3 describes the data reduction and analysis procedures for the *NuSTAR* observations. Section 4 focuses on the results of SC on the full BAT sample of 241 nearby AGNs ($z < 0.03$), a subset of 84/241 *NuSTAR*-observed AGNs, and the X-ray spectral and multiwavelength analyses for the nine *NuSTAR*-observed SC-selected AGNs. Finally, Section 5 gives a summary of our results and discusses the implications of the full survey in terms of the black hole growth. Throughout this work, we adopt $\Omega_m = 0.27$, $\Omega_\Lambda = 0.73$, and $H_0 = 71 \text{ km s}^{-1} \text{ Mpc}^{-1}$. Errors are quoted at the 90% confidence level unless otherwise specified.

2. SAMPLE SELECTION

Here we describe the simulations used to derive the SC measurement in *Swift*/BAT and *NuSTAR* data (Section 2.1). We then discuss the results of applying this SC measurement to nearby *Swift*/BAT AGNs (Section 2.2). Finally, we select nine high SC BAT AGNs for *NuSTAR* follow-up.

2.1. SC Measurement

We define a curvature parameter to estimate Compton thickness using the distinctive spectral shape created by Compton reflection and scattering (Figure 1). We hereafter call it the SC. We generated the simulated data (using the XSPEC *fakeit* feature) from Compton-thick obscuration using the MYTORUS model (Murphy & Yaqoob 2009).

The MYTORUS-based model used for calculating the SC (Model SC hereafter) has the following form:

$$\text{Model SC} = \text{MYTZ} \times \text{POW} + \text{MYTS} + \text{MYTL}.$$

Here, MYTZ represents the zeroth-order transmitted continuum (POW) through photoelectric absorption and the Compton scattering of X-ray photons out of the line of sight, MYTS is the scattered/reflected continuum produced by scattering X-ray photons into the line of sight, and MYTL is the fluorescent emission-line spectrum. The torus model we use for measuring SC is viewed nearly edge-on ($\theta_{\text{inc}} = 80^\circ$) with a cutoff power law ($\Gamma = 1.9$, $E_c > 200 \text{ keV}$). The SC model assumes a half opening angle of 60° , which is equivalent to a covering factor of 0.5. The SC is calculated so that a heavily Compton-thick source in an edge-on torus model has a value of 1 (e.g., SC = 1

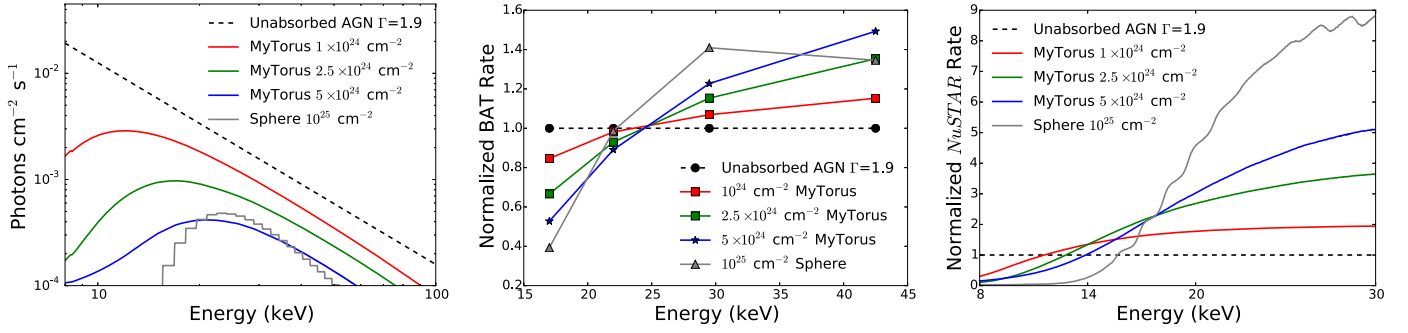


Figure 1. Left: simulated Compton-thick AGNs compared to an unabsorbed power-law source with $\Gamma = 1.9$ showing the increasing SC with column density. Center: *Swift*/BAT count rates for these same sources normalized by the rate of an unobscured source for the four BAT channels between 14 and 50 keV. The energy bands above 24 keV show an excess, while the bands between 14 and 24 keV show a decrement. Right: *NuSTAR* count rates for these same sources normalized by the rate of an unobscured source in the range 8–30 keV. At energies between 14 and 30 keV, a Compton-thick source has an excess, while the 8–14 keV energy band shows a decrement compared to the count rates of an unobscured source. The weighted average of BAT and *NuSTAR* energy bands can be used to find Compton-thick sources.

for $N_{\text{H}} = 5 \times 10^{24} \text{ cm}^{-2}$) and an unabsorbed AGN has a value of 0.

The SC can be applied to X-ray observations from any satellite with energy coverage of the “Compton hump” (≈ 10 –30 keV). This “hump” occurs because of the energy dependence of photoelectric absorption, whereby soft X-rays are mostly absorbed, and higher-energy photons are rarely absorbed and tend to Compton scatter (see, e.g., Reynolds 1999). The SC measurement uses weighted averages of different energy ranges as compared to the count rate in an unobscured AGN. To estimate the SC for BAT data, we focus on data below 50 keV because this shows the strongest difference in curvature compared to an unobscured source. Additionally, the BAT sensitivity is significantly reduced in the 50–195 keV energy ranges. For *NuSTAR*, we use the 8–14 keV, 14–20 keV, and 20–30 keV energy ranges, because of the reduced sensitivity of *NuSTAR* above 30 keV compared to the preceding energy ranges. We note that the SC method will be biased against Compton-thick AGNs with very high column densities ($N_{\text{H}} > 5 \times 10^{24} \text{ cm}^{-2}$) because of the large reduction in count rates (Figure 2).

The two SC equations take the following form:

$$\text{SC}_{\text{BAT}} = \frac{-3.42 \times A - 0.82 \times B + 1.65 \times C + 3.58 \times D}{\text{Total Rate}}, \quad (1)$$

where A , B , C , and D refer to the 14–20 keV, 20–24 keV, 24–35 keV, and 35–50 keV channel *Swift*/BAT count rates, respectively, and the total rate refers to the 14–50 keV total rate; and

$$\text{SC}_{\text{NuSTAR}} = \frac{-0.46 \times E + 0.64 \times F + 2.33 \times G}{\text{Total Rate}} \quad (2)$$

where E , F , and G refer to the *NuSTAR* 8–14 keV, 14–20 keV, and 20–30 keV on-axis count rates, respectively, and the total rate refers to the 8–30 keV total rate in the A and B telescope. Simulations of the SC measurement with *Swift*/BAT and *NuSTAR*, as well as different model parameters and column densities, are shown in Figure 3. The differences between SC measurements at a specific column density using a variety of different torus model parameters or using *NuSTAR* or *Swift*/BAT are small except at very high column densities ($N_{\text{H}} > 4 \times 10^{24} \text{ cm}^{-2}$). The SC measure is more sensitive to sources that are mildly Compton-thick ($N_{\text{H}} \approx$

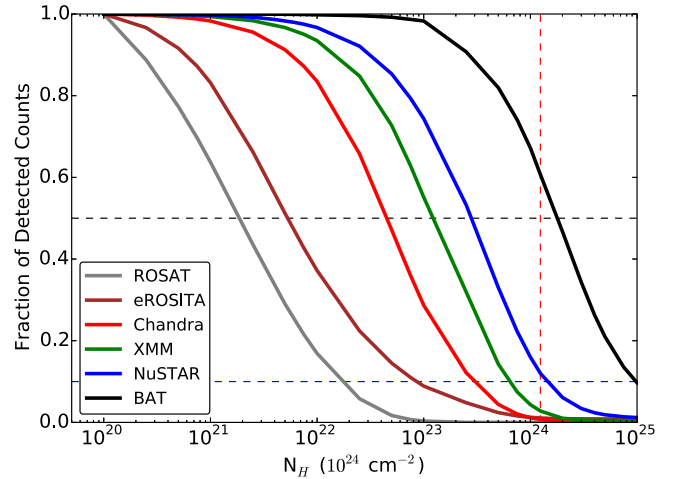


Figure 2. Simulations using an edge-on MYTorus model showing the reduction in count rates for instruments observing AGNs of different column densities. The black and blue horizontal dashed lines indicate a 50% and 90% reduction, respectively. Surveys below 10 keV like *ROSAT* and *eROSITA* are strongly biased against detecting heavily obscured AGNs, and *Chandra* and *XMM-Newton* are heavily biased against detecting Compton-thick AGNs, while *NuSTAR* and *Swift*/BAT are less biased against Compton-thick AGNs with very high column densities ($N_{\text{H}} > 5 \times 10^{24} \text{ cm}^{-2}$) because of the large reduction in count rates.

$3 \times 10^{24} \text{ cm}^{-2}$), as can be seen by the flattening of the slope at very high column densities. As SC_{BAT} only uses emission above 14 keV, it is insensitive to differences between unobscured sources and mildly obscured sources ($N_{\text{H}} < 7 \times 10^{23} \text{ cm}^{-2}$) that fail to obscure any of the softest 14–20 keV emission. Finally, we show simulations of broad-band ratios that, unlike the SC measurement, are ineffective at selecting Compton-thick AGNs because of a degeneracy with sources at lower column densities.

2.2. SC of Nearby BAT AGNs and *NuSTAR* Targets

We applied the SC to study Compton thickness in a sample of nearby ($z < 0.03$) BAT-detected AGNs. We use the 70-month catalog (Baumgartner et al. 2013) with a low-luminosity cut ($L_{14-195 \text{ keV}} > 10^{42} \text{ erg s}^{-1}$) to avoid detecting purely star-forming galaxies such as M82. This luminosity limit corresponds to the 90% BAT all-sky sensitivity limit at 100 Mpc ($z = 0.023$), so that our survey sensitivity is more uniform in the volume explored. This does exclude one lower-

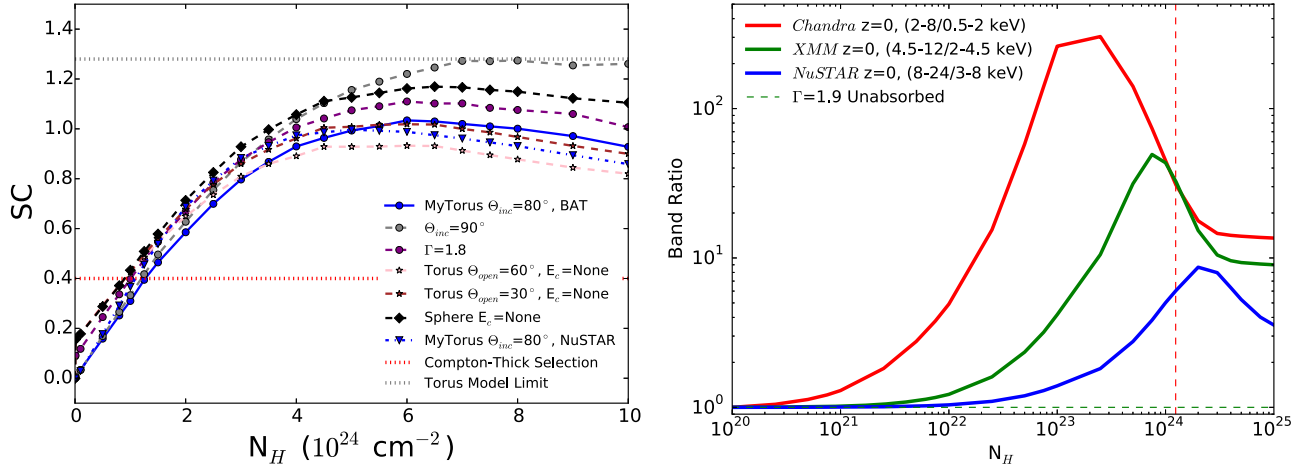


Figure 3. Left: variations in SC with column density based on XSPEC simulations. The blue solid line shows the MYTORUS model used for the SC_{BAT} definition with $\Gamma = 1.9$, $E_c = 200$ keV, and $\theta_{inc} = 80^\circ$. SC_{NuSTAR} (blue dashed line) only shows small differences from SC_{BAT} ($\Delta SC < 0.07$) at all column densities. We also show the dependency of SC_{BAT} on inclination angle (θ_{inc} , gray circle), intrinsic power law (Γ , purple circle), opening angle with BNTORUS model (θ_{open} , pink and brown stars; Brightman & Nandra 2011), or a simple sphere model (black diamonds; Brightman & Nandra 2011). The differences between models are small ($\Delta SC_{BAT} < 0.1$) except at very high column densities ($N_H > 4 \times 10^{24} \text{ cm}^{-2}$). At very high column densities ($N_H > 4 \times 10^{24} \text{ cm}^{-2}$) the SC measure does not increase at larger column densities. At low column densities ($N_H < 5 \times 10^{23} \text{ cm}^{-2}$), the lack of the high-energy cutoff in the BNTORUS and sphere models raises the SC because of the additional flux in the high-energy emission. A red dotted line shows the Compton-thick lower limit ($SC_{BAT} = 0.4$) used for this study, and a gray dotted line shows the upper limit from the torus model ($SC_{BAT} = 1.28$). Right: simulations of obscured sources using band ratios. The band ratio, unlike the SC method, is ineffective at selecting Compton-thick AGNs because of a degeneracy with sources at lower column densities.

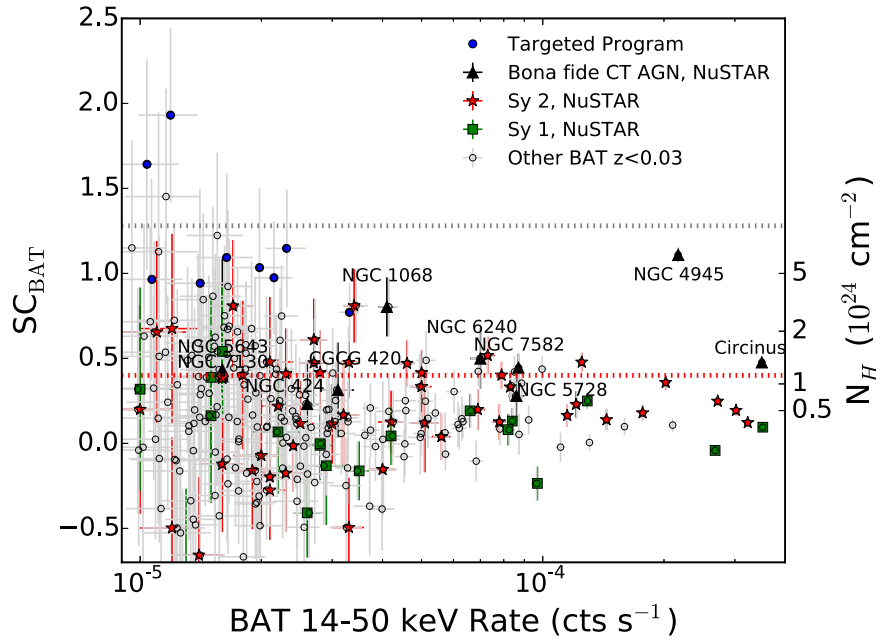


Figure 4. SC measurement for our sample of 241 BAT AGNs at $z < 0.03$. Compton-thick AGNs confirmed with NuSTAR are shown in black, mildly obscured Seyfert 2s observed with NuSTAR are shown in red, and NuSTAR-observed Seyfert 1s are shown in green. The simulation upper limits of any torus model are shown as a horizontal gray dotted line, while a Compton-thick column is shown by a horizontal red dotted line. The SC-selected NuSTAR targets in our program (blue) were selected to have the highest SC measure along with archival optical imaging and spectroscopy. The majority of the NuSTAR program is at much fainter fluxes than previously known Compton-thick AGNs.

luminosity ($L_{14-195 \text{ keV}} < 10^{42} \text{ erg s}^{-1}$) BAT-detected Compton-thick AGN (NGC 4102). We also exclude four sources in the Galactic plane with heavy obscuration ($E[B - V] > 1.2$, galactic latitude $|b| < 10^\circ$) because of the difficulty of multi-wavelength study, as well as eight BAT detections that are heavily contaminated by a secondary BAT source. The final sample includes 241 BAT-detected nearby AGNs. Of these, 35% (84/241) have been observed by NuSTAR.

We measure the SC in these 241 BAT AGNs (Figure 4). We have highlighted 10 “bona fide” Compton-thick AGNs in our

sample that have been observed with NuSTAR and have been confirmed to be Compton-thick based on spectral fitting (Gandhi et al. 2014). We targeted nine northern hemisphere objects with archival optical imaging and spectroscopy from past studies (e.g., Koss et al. 2011b, 2012) and very high SC values for NuSTAR follow-up. Two of the nine targeted NuSTAR sources have measured curvatures above simulation upper limits. The majority of our sample is at much fainter fluxes than previously known Compton-thick AGNs observed by NuSTAR (e.g., Arévalo et al. 2014; Baloković et al. 2014;

Table 1
Likely Compton-thick AGNs Using Spectral Curvature

Object	Type ^a	Sey. ^b	z ^c	SC _{BAT}	SC _{NUSTAR} ^d	BAT 14–50 keV ^e
NGC 6232	P	2	0.015	1.93 ± 0.51	0.27 ± 0.14	1.19E-05
CGCG 164-019	P	1.9	0.030	1.64 ± 0.62	0.39 ± 0.06	1.04E-05
ESO 406-G004	...	2	0.029	1.45 ± 0.63	...	1.16E-05
MCG +00-09-042	...	2	0.024	1.22 ± 0.49	...	1.55E-05
NGC 3393	P	2	0.013	1.15 ± 0.35	0.77 ± 0.04	2.31E-05
ESO 323-32	...	2	0.016	1.13 ± 0.82	...	1.11E-05
NGC 4945	CTB	2	0.002	1.11 ± 0.04	1.01 ± 0.01	2.17E-04
MCG +06-16-028	P	1.9	0.016	1.09 ± 0.50	0.56 ± 0.04	1.64E-05
UGC 3157	P	2	0.015	1.03 ± 0.47	0.28 ± 0.04	1.98E-05
2MFGC 02280	P	2	0.015	0.97 ± 0.33	0.73 ± 0.07	2.15E-05
NGC 3588 NED01	P	2	0.026	0.96 ± 0.59	0.26 ± 0.04	1.07E-05
NGC 7212 NED02	P	2	0.027	0.94 ± 0.55	0.35 ± 0.04	1.41E-05
NGC 1106	...	2	0.015	0.92 ± 0.45	...	1.65E-05
ESO 565-G019	...	2	0.016	0.87 ± 0.53	...	1.52E-05
CGCG 229-015	...	1.5	0.028	0.85 ± 0.51	...	1.43E-05
NGC 1194	...	2	0.014	0.81 ± 0.22	0.56 ± 0.03	3.44E-05
2MASX J07262635-3554214	...	2	0.029	0.81 ± 0.39	0.37 ± 0.03	1.71E-05
NGC 1068	CTB	2	0.004	0.80 ± 0.17	0.66 ± 0.02	4.15E-05
NGC 3079	P	1.9	0.004	0.77 ± 0.17	0.87 ± 0.04	3.31E-05
UGC 12282	...	2	0.017	0.75 ± 0.41	...	1.62E-05
ESO 426-G002	...	2	0.022	0.75 ± 0.30	...	2.25E-05
ESO 005-G004	...	2	0.006	0.61 ± 0.24	...	2.72E-05
UGC 12741	...	2	0.017	0.61 ± 0.31	...	2.23E-05
MCG +04-48-002	...	2	0.014	0.52 ± 0.11	0.45 ± 0.04	7.29E-05
NGC 6240	CTB	1.9	0.025	0.50 ± 0.18	0.50 ± 0.02	6.98E-05
Fairall 51	...	1.5	0.014	0.49 ± 0.18	...	5.13E-05
Mrk 3	CTB	1.9	0.014	0.48 ± 0.05	0.35 ± 0.01	1.25E-04
Circinus Galaxy	CTB	2	0.001	0.48 ± 0.03	0.69 ± 0.01	3.50E-04
NGC 612	...	2	0.030	0.47 ± 0.13	0.39 ± 0.03	4.61E-05
NGC 7582	CTB	2	0.005	0.45 ± 0.08	0.39 ± 0.02	8.71E-05
NGC 3281	...	2	0.011	0.44 ± 0.08	...	9.96E-05
ESO 297-018	...	2	0.025	0.42 ± 0.09	...	6.92E-05
NGC 3081	...	2	0.008	0.42 ± 0.09	...	8.50E-05
NGC 1365	...	2	0.006	0.40 ± 0.08	0.26 ± 0.01	7.92E-05
ARP 318	...	2	0.013	0.72 ± 0.57	...	1.22E-05
UGC 07064	...	1.9	0.025	0.72 ± 0.55	...	1.06E-05
HE 1136-2304	...	1.9	0.027	0.69 ± 0.51	...	1.66E-05
NGC 452	...	2	0.017	0.68 ± 0.43	...	1.62E-05
NGC 7479	...	1.9	0.008	0.68 ± 0.40	...	1.89E-05
MCG -01-30-041	...	1.8	0.019	0.67 ± 0.46	...	1.65E-05
NGC 2788A	0.013	0.66 ± 0.38	...	1.75E-05
CGCG 122-055	...	1.5	0.021	0.63 ± 0.66	...	1.02E-05
Mrk 1310	...	1.5	0.019	0.62 ± 0.49	...	1.54E-05
NGC 7465	...	2	0.007	0.59 ± 0.52	...	1.39E-05
NGC 1125	...	2	0.011	0.58 ± 0.36	...	1.83E-05
NGC 3035	...	1.5	0.015	0.57 ± 0.40	...	1.93E-05
ESO 553-G043	...	2	0.028	0.57 ± 0.45	...	1.53E-05
NGC 3786	...	1.9	0.009	0.54 ± 0.38	0.09 ± 0.05	1.55E-05
ESO 317-G038	...	2	0.015	0.54 ± 0.65	...	1.16E-05
UGC 11397	...	2	0.015	0.53 ± 0.42	...	1.83E-05
ESO 374-G044	...	2	0.028	0.52 ± 0.46	...	1.64E-05
ESO 533-G050	...	2	0.026	0.51 ± 0.70	...	1.11E-05
PKS 2153-69	...	2	0.028	0.51 ± 0.48	...	1.48E-05
NGC 7679	...	1.9	0.017	0.50 ± 0.44	...	1.71E-05
Mrk 622	...	1.9	0.023	0.49 ± 0.55	...	1.31E-05
UGC 03995A	...	2	0.016	0.48 ± 0.38	0.36 ± 0.02	2.06E-05
NGC 7319	...	1.9	0.023	0.48 ± 0.21	0.40 ± 0.07	3.29E-05
MCG -01-05-047	...	2	0.017	0.47 ± 0.26	0.28 ± 0.03	2.71E-05
Mrk 590	...	1.5	0.026	0.44 ± 0.41	...	1.71E-05
NGC 6552	...	2	0.027	0.44 ± 0.34	...	1.83E-05
ESO 549-G049	...	1.9	0.026	0.44 ± 0.31	...	2.18E-05
NGC 5643	CTB	2	0.004	0.43 ± 0.65	0.47 ± 0.05	2.18E-05
2MASX J07394469-3143024	...	2	0.026	0.42 ± 0.25	0.25 ± 0.02	2.80E-05
NGC 4992	...	2	0.025	0.42 ± 0.13	0.30 ± 0.02	5.02E-05

Table 1
(Continued)

Object	Type ^a	Sey. ^b	z^c	SC _{BAT}	SC _{NuSTAR} ^d	BAT 14–50 keV ^e
CGCG 367-009	...	2	0.027	0.41 ± 0.27	0.10 ± 0.03	2.32E-05
2MASX J18263239+3251300	...	2	0.022	0.40 ± 0.44	0.07 ± 0.01	1.78E-05
NGC 7130	CTB	1.9	0.016	0.40 ± 0.55	0.86 ± 0.08	1.56E-05
CGCG 420-015	CTB	1.9	0.029	0.31 ± 0.28	0.44 ± 0.03	3.08E-05
NGC 5728	CTB	2	0.009	0.28 ± 0.14	0.61 ± 0.02	8.56E-05
NGC 424	CTB	1.9	0.012	0.23 ± 0.25	0.58 ± 0.05	2.58E-05
2MASX J00253292+6821442	...	2	0.012	-0.1 ± 0.40	0.56 ± 0.05	1.59E-05

Notes. List of likely Compton-thick AGNs based on SC from our BAT sample of 241 $z < 0.03$ AGNs. The errors indicated here are 1σ . The upper section lists any likely Compton-thick BAT AGNs (34/241; SC_{BAT} > 0.4 and an error lower bound of SC_{BAT} > 0.3). The middle section lists the remaining sources with SC_{BAT} > 0.4, which are less likely to be Compton-thick (33/241) because of the large error bars. Finally, the bottom section shows four sources with SC > 0.4 in *NuSTAR*, but SC_{BAT} < 0.4.

^a Type of AGN: P—SC-selected BAT AGNs observed in our *NuSTAR* program; CTB—“bona fide” Compton-thick AGNs confirmed to be Compton-thick based on spectral fitting (Gandhi et al. 2014); U—above upper limit in SC_{BAT} for torus simulations.

^b AGN type based on optical spectra from Koss et al. (2016) or NED.

^c Measured redshift from NED.

^d Where ellipses are shown, no public *NuSTAR* observations exist.

^e BAT 14–50 keV total count rate in counts s⁻¹. Total count rate errors are small ($< 3 \times 10^{-6}$ counts s⁻¹).

Bauer et al. 2014; Puccetti et al. 2014; Brightman et al. 2015). A list of likely Compton-thick AGNs based on SC is found in Table 1.

The brightest three targets from the *NuSTAR* SC program (NGC 3079, NGC 3393, and NGC 7212) have already been claimed to be Compton-thick, but we observed them for the first time with *NuSTAR* to confirm this. NGC 3079 was suggested to be Compton-thick based on a large Fe K α equivalent width (> 1 keV) and prominent emission above 10 keV with *BeppoSAX* (Iyomoto et al. 2001). For NGC 3393, *BeppoSAX* observations in 1997 suggested column densities of $N_{\text{H}} = 3 \times 10^{23}$ cm⁻², but the large Fe K α line equivalent width (> 1 keV), high ratio of [O III] to soft X-ray flux, and a > 20 keV excess suggested a Compton-thick AGN (Salvati et al. 1997). Risaliti et al. (2000) suggested that NGC 7212 is Compton-thick from analysis of a low signal-to-noise ratio *ASCA* spectrum, based on a flat continuum and a prominent Fe K α line.

The remaining six targets (2MFGC 02280, CGCG 164-019, MCG +06-16-028, NGC 3588 NED0201, NGC 6232, and UGC 3157) have never been suggested to be Compton-thick in past literature. They were first observed with *Swift*/XRT for BAT counterpart identification. 2MFGC 02280 (SWIFT J0251.3+5441) was observed for 10.9 ks, with no counterpart detected above 3σ in the BAT error circle (Baumgartner et al. 2013). The remaining five sources were observed for 8–13 ks and confirmed to be the brightest X-ray source within the BAT error circle. Most of these AGNs are just above the BAT detection limit of 4.8σ (NGC 3588 S/N = 5.0, CGCG 164-019 S/N = 5.1, MCG +06-16-028 S/N = 6.1, NGC 6232 S/N = 5.1, UGC 3157 S/N = 5.4), with a more significant detection of 2MFGC 02280 (S/N = 8.9). Of these, only NGC 3588 NED02 was observed using *Chandra*, in a study searching for dual AGNs in close mergers (Koss et al. 2012).

3. DATA AND REDUCTION

3.1. NuSTAR

Table 2 provides details, including dates and exposure times, for the nine *NuSTAR* observations of SC-selected BAT AGNs.

We analyzed these sources, as well as 75 other low-redshift ($z < 0.03$) AGNs in the *NuSTAR* public archive, for a total of 84 *NuSTAR* observations. We have chosen not to include the *Swift*/BAT data in the model fits because our selection method will bias our fits to Compton-thick obscuration and the *Swift*/BAT data were taken over a period of 6 yr (2004–2010).

The raw data were reduced using the NuSTARDAS software package (version 1.3.1) jointly developed by the ASI Science Data Center and the California Institute of Technology. NuSTARDAS is distributed with the HEASoft package by the NASA High Energy Astrophysics Archive Research Center. We extracted the *NuSTAR* source and background spectra using the nuproducts task included in the NuSTARDAS package using the appropriate response and ancillary files. Spectra were extracted from circular regions 40'' in radius, centered on the peak of the centroid of the point-source images. The background spectra were extracted from a circular region lying on the same detector as the source. We also applied the same reduction procedure to the other 75 low-redshift ($z < 0.03$) *NuSTAR*-observed AGNs in the public archive for SC_{NuSTAR} measurements of a total of 84 *NuSTAR*-observed nearby BAT-detected AGNs.

3.2. Soft X-Ray Observations of SC-selected AGNs

Most *NuSTAR* observations were accompanied by a short observation (3–7 ks) with *Swift*/XRT within 24 hr, although for one source, UGC 3157, the only available observation was from 4 yr earlier. These observations provided mostly simultaneous coverage in the soft X-rays (< 3 keV), where *NuSTAR* is not sensitive. All the *Swift*/XRT data were collected in Photon Counting mode. We built *Swift*/XRT spectra using the standard point-source processing scripts from the UK *Swift* Science Data Centre in Leicester (Evans et al. 2009). Table 2 provides the complete list of observations. The *Swift*/XRT observations of 2MFGC 02280 and NGC 3588 NED02 did not yield a detection below 3 keV, so we use them here only to place an upper limit on the soft X-ray emission.

In addition to the *NuSTAR* and *Swift*/XRT data, there are archival *XMM-Newton* (for NGC 3079 and NGC 7212

Table 2
X-Ray Observation Log

Object Name (1)	BAT ID (2)	z (3)	<i>NuSTAR</i> Observations			XRT Observations		
			Observation ID (4)	UT Date (5)	t_{eff} (6)	Observation ID (7)	UT Date (8)	t (9)
2MFGC 02280	SWIFT J0251.3+5441	0.0152	60061030002	2013 Feb 16	15	00080255001	2013 Feb 16	6
CGCG 164-019	SWIFTJ1445.6+2702	0.0299	60061327002	2013 Sep 13	24	00080536001	2013 Sep 13	6
MCG +06-16-028	SWIFTJ0714.2+3518	0.0157	60061072002	2013 Dec 03	23	00080381001	2013 Dec 03	7
NGC 3079	SWIFTJ1001.7+5543	0.0037	60061097002	2013 Nov 12	21	00080030001	2013 Nov 12	6
NGC 3393	SWIFTJ1048.4+2511	0.0125	60061205002	2013 Jan 28	15	00080042001	2013 Jan 28	7
NGC 3588 NED02	SWIFTJ1114.3+2020	0.0262	60061324002	2014 Jan 17	23	00080533001	2014 Jan 17	5
NGC 6232	SWIFTJ1643.2+7036	0.0148	60061328002	2013 Aug 17	18	00080537001	2013 Aug 17	6
NGC 7212 NED02	SWIFTJ2207.3+1013	0.0267	60061310002	2013 Sep 01	24	00080283001	2013 Sep 02	3
UGC 3157	SWIFTJ0446.4+1828	0.0154	60061051002	2014 Mar 18	20	00041747001	2010 Oct 22	10

Note. (1) Full NED object name for BAT counterpart. (2) *Swift*/BAT name. (3) Redshift. (4) and (5) *NuSTAR* observation ID and start date (YYYY-MM-DD), respectively. (6) Effective exposure time (ks). This is the net value after data cleaning and correction for vignetting. (7) and (8) *Swift*/XRT observation ID and start date (YYYY-MM-DD), respectively. (9) Net on-axis, flaring-corrected exposure time (ks).

NED02) and *Chandra* data available (for NGC 3393 and NGC 3588 NED02). Studies of NGC 3079, NGC 7212, and NGC 3393 found no signs of variability (Hernández-García et al. 2015; Koss et al. 2015), so we use these spectra because of their much higher sensitivity than *Swift*/XRT. For NGC 3588 NED02, the source is very faint with a total of 9 counts, all above 3 keV, in the *Swift*/XRT observation, compared to 72 counts in the *Chandra* observation. We fit the *Chandra*, *NuSTAR*, and *Swift*/XRT spectra between 3 and 8 keV with a power law and a cross-normalization factor for the *Chandra* data. We find that *Chandra* is consistent with no variability (1.2 ± 0.5).

We processed the *XMM-Newton* observations using the Science Analysis Software, version 13.5.0, with the default parameters of *xmextractor*. NGC 3079 had two *XMM-Newton* observations, which we combined using *epicscombine* for a total exposure time of 9.4 ks after filtering. After filtering, NGC 7212 had an exposure time of 9.3 ks. We also used *epicscombine* to combine the MOS1 and MOS2 instruments into a single spectrum before fitting. We reduced and combined the two *Chandra* observations of NGC 3393, with a total exposure of 99.9 ks, and NGC 3588 NED02, with a total exposure of 9.9 ks, following Koss et al. (2015).

3.3. X-Ray Spectral Fitting

For the three brightest sources with *XMM-Newton* and *Chandra* data, NGC 3079, NGC 7212 NED02, and NGC 3393, we binned to a minimum of 20 photons per bin using the *HEASOFT* task *grppha*. We use *statisticstest* (Wachter et al. 1979) in *XSPEC* for the remaining six sources, which is more appropriate than χ^2 in the case of Poisson-distributed data (Nousek & Shue 1989). In the case of unmodeled background spectra, *cstat* applies the *W* statistic.¹⁹ While the *W* statistic is intended for unbinned data, bins containing zero counts can lead to erroneous results,²⁰ so we group the *Swift*/XRT and *NuSTAR* data by a minimum of

3 counts per bin, respectively (e.g., Wik et al. 2014), using the *HEASOFT* task *grppha*.

We let the *Swift*/XRT and *NuSTAR* FPMA and FPMB cross-normalizations vary independently within 5% based on the most recent calibrations (Madsen et al. 2015). We also use varying cross-normalizations of 0.93 ± 0.05 for *Chandra*, 1.05 ± 0.05 for *XMM-Newton* pn, and 1.02 ± 0.05 for the combined MOS observation based on recent *NuSTAR* calibrations.

Conventional spectral fitting and error estimation can sometimes underestimate the likely range of model parameters. Additionally, several past studies have found degeneracies between photon index (Γ) and column density (N_{H}) for *NuSTAR*-observed Compton-thick AGNs (e.g., Gandhi et al. 2014). We therefore use Markov chain Monte Carlo methods built into *XSPEC* for error estimation. We use the default Goodman–Weare algorithm to sample parameter space, constructing a chain of parameter values. The algorithm works by holding multiple sets of parameters, called walkers, for each step in the chain and generating walkers for the next step using those from the current step.

3.4. X-Ray Spectral Modeling

For spectral modeling, we follow the strategies of past studies of a single AGN observed with *NuSTAR* (e.g., Gandhi et al. 2014) and use the *MYTORUS* and *BNTORUS* models. Since the soft X-ray data (<3 keV) from *Swift*/XRT typically have a small number of counts (≈ 0 –30) and therefore lack the statistics to model this emission in detail, we use two components corresponding to scattered AGN emission on larger scales in the host galaxy and a thermal plasma. In the absence of high signal-to-noise ratio and spectral resolution soft X-ray data, these are only meant as a simple prescription to describe the spectral shape in this regime. The scattered emission was simulated using a single power law (of photon index Γ and normalization tied to that of the AGN) and with a scattering fraction, f_{scatt} , relative to the intrinsic power law. We also include a low-energy component with a thermal plasma component (*APEC*; Smith et al. 2001), fixing the abundance to solar, similar to past studies (e.g., Guainazzi et al. 1999).

¹⁹ See also <http://heasarc.gsfc.nasa.gov/docs/xanadu/xspec/wstat.ps>.

²⁰ See <https://heasarc.gsfc.nasa.gov/xanadu/xspec/manual/XSappendixStatistics.html>.

The MYTORUS-based model (Model M hereafter) has the following form:

$$\begin{aligned} \text{Model M} = & \text{PHABS} \times (\text{MYTZ} \times \text{POW} \\ & + f_{\text{refl}} * (\text{MYTS} + \text{MYTL}) \\ & + f_{\text{scatt}} * \text{POW} + \text{APEC}). \end{aligned}$$

The common parameters of MYTZ, MYTS, and MYTL (N_{H} and θ_{inc}) are tied together. N_{H} is defined along the equatorial plane of the torus. There is a fitted constant (f_{refl}) between the zeroth-order continuum and the scattered/reflected and fluorescent emission-line spectrum. The intrinsic (unprocessed) photon indices and normalizations are tied to those of the zeroth-order continuum (POW). The torus opening angle (θ_{tor}) is fixed at 60° in the current version of MYTORUS.

Our second choice of physically motivated model (Model T hereafter) uses the BNTORUS model and has the following form:

$$\begin{aligned} \text{Model T} = & \text{PHABS} \times (\text{BNTORUS} \\ & + f_{\text{scatt}} * \text{POW} + \text{APEC}). \end{aligned}$$

BNTORUS self-consistently includes photoelectric absorption, Compton scattering, and fluorescent line emission due to the obscuration of an intrinsic power-law continuum by a biconical torus (Brightman & Nandra 2011), so no f_{refl} factor is used in this model. N_{H} is defined along the line of sight and is independent of θ_{inc} .

4. RESULTS

Here we discuss our results measuring the SC for the full BAT sample of 241 nearby AGNs, as well as a subset of 84/241 *NuSTAR*-observed nearby BAT AGNs (Section 4.1). We then discuss results for the nine *NuSTAR*-observed SC-selected AGNs, focusing on simple and complex X-ray spectral fits (Section 4.2). Next, we examine other measurements of Compton thickness using the mid-IR and [O III] emission (Section 4.3). We conclude with a comparison of the host galaxy properties and accretions rates compared to all BAT-detected nearby AGNs (Section 4.4).

4.1. Spectral Curvature

The SC measure may be used to measure the overall fraction of Compton-thick sources and whether the curvature of these sources is consistent with torus models. Using SC_{BAT} , about $28\% \pm 5\%$ (67/241) of AGNs fall within the Compton-thick region (Figure 4). However, the large error bars of SC_{BAT} at low fluxes ($< 3 \times 10^{-5}$ counts s^{-1}) may overestimate this fraction because of the larger number of sources below the limit. A more conservative estimate using only bright sources ($> 3 \times 10^{-5}$ counts s^{-1}) finds a Compton-thick fraction of $22\% \pm 8\%$ (18/79), which is lower than, but not statistically different from, the fraction for the whole sample. We note that both of these fractions are broadly consistent with a recent publication of the intrinsic fraction of Compton-thick AGNs in the entire BAT sample ($27 \pm 4\%$, Ricci et al. 2015). The SC_{BAT} identifies most well-known Compton-thick AGNs in the “bona fide” sample (7/10), with the remaining three identified within their 1σ error.

We can also estimate the local Compton-thick space density. Assuming a luminosity threshold of $L_{2-10 \text{ keV}} > 10^{43}$ erg s^{-1} and a conversion factor between 14–195 keV and

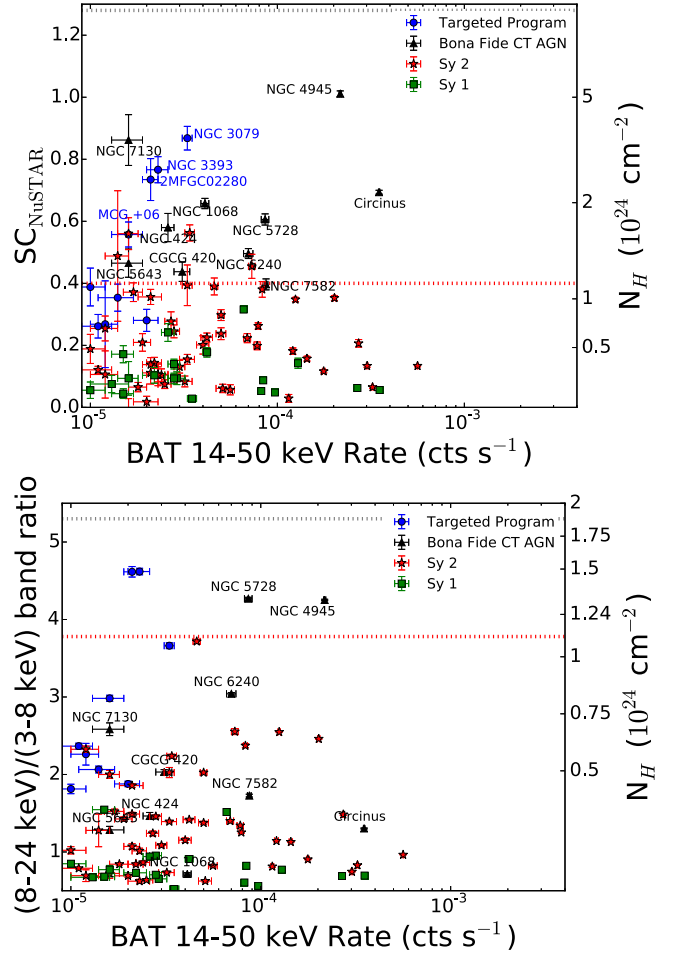


Figure 5. Top: plot of the SC_{NuSTAR} measurement for nearby ($z < 0.03$) BAT AGNs. The nine BAT AGNs targeted based on 14–50 keV curvature are shown in blue. Well-known “bona fide” Compton-thick AGNs observed with *NuSTAR* are shown in black. The simulation limits for an edge-on torus are shown as a gray dotted line, while the lower limit of a Compton-thick column is shown by a red dotted line. Bottom: band ratios of BAT AGNs observed with *NuSTAR* (8–24 keV/3–8 keV).

2–10 keV of 2.67 (Rigby et al. 2009), we find 74 BAT AGNs. We estimate that 16 are Compton-thick ($SC_{\text{BAT}} > 0.4$). Given that the sample is within $z < 0.03$ excluding the 10° within the Galactic plane and confused sources, and the 91% completeness at this luminosity threshold (Baumgartner et al. 2013), this implies a volume of $7.0 \times 10^6 \text{ Mpc}^3$. The Compton-thick number density is therefore $(2.3 \pm 0.3) \times 10^{-6} \text{ Mpc}^{-3}$ above $L_{2-10 \text{ keV}} > 10^{43}$ erg s^{-1} .

The higher sensitivity of *NuSTAR* allows a more precise SC measurement than *Swift*/BAT because of the higher sensitivity. We measure SC_{NuSTAR} for those nearby AGNs with *NuSTAR* observations (35%, 84/241; Figure 5). While the SC measurements are designed to be independent of the telescope, *NuSTAR* is studying a somewhat softer energy range because of its reduced sensitivity above 30 keV (14–50 keV vs. 8–30 keV). Thus, the two SC measurements may have systematically different average values. However, for the sample of 84 overlapping sources $SC_{\text{BAT}} = 0.29 \pm 0.07$ and $SC_{\text{NuSTAR}} = 0.27 \pm 0.03$, showing no evidence of a significant difference, at least on average. We can also compare our SC measurements for “bona fide” *NuSTAR*-observed Compton-thick AGNs that were confirmed based on spectral fitting

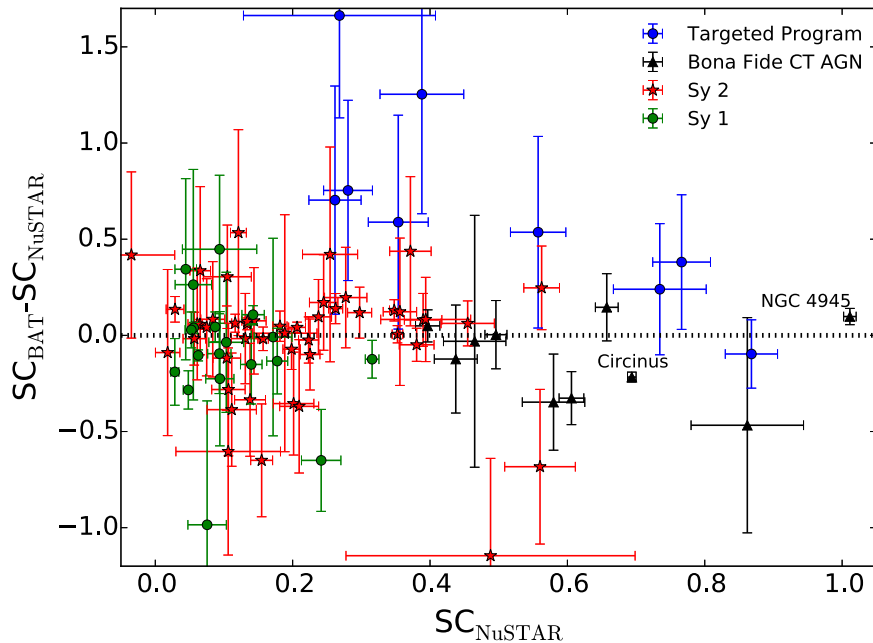


Figure 6. Comparison of SC measurement for all 84 BAT AGNs with *NuSTAR* observations. Compton-thick AGNs confirmed with *NuSTAR* are shown in black, mildly obscured Seyfert 2s observed with *NuSTAR* are shown in red, and *NuSTAR*-observed Seyfert 1s are shown in green. A horizontal black dotted line is plotted through zero. The two measurements show no significant difference on average ($SC_{\text{BAT}} = 0.29 \pm 0.05$ and $SC_{\text{NuSTAR}} = 0.27 \pm 0.02$).

(Gandhi et al. 2014). We find that the Compton-thick fraction estimated using SC_{NuSTAR} is also similar ($21\% \pm 7\%$, 16/84) to the SC_{BAT} measurement.

We also look for individual sources whose SC_{BAT} and SC_{NuSTAR} measurements differ significantly (Figure 6). The SC_{BAT} is based on time average spectra over 6 yr between 2004 November and 2010 August, which may differ from the *NuSTAR* observations, which occurred after 2012. We look for sources above 2.6σ , where we expect only one source from statistical noise with a sample size of 84. We find five sources whose change ($SC_{\text{BAT}} - SC_{\text{NuSTAR}}$) was greater than 2.6σ . The majority of these are Seyfert 1s, which are already known to be variable above 10 keV based on *NuSTAR* (MCG -06-30-015, MCG -05-23-016, NGC4151; Parker et al. 2014; Baloković et al. 2015; Keck et al. 2015). Another source with a significant difference is Circinus. However, analysis of the *NuSTAR* and *Swift*/BAT spectra found that the 14–20 keV *Swift*/BAT energy band was significantly contaminated by a nearby ULX, which would explain the lower value of SC_{BAT} compared to SC_{NuSTAR} (Arévalo et al. 2014). The final source is NGC 6232, one of the program sources, whose SC_{NuSTAR} was 3.1σ below SC_{BAT} . Further *NuSTAR* observations would be necessary to confirm whether this source is variable.

We can also test whether the *NuSTAR* SC or a broadband ratio (8–24 keV/3–8 keV) is more efficient at finding Compton-thick AGNs. For the well-known Compton-thick AGNs observed with *NuSTAR*, all (10/10) are found in the Compton-thick region of the 8–30 keV SC measurement. This is an improvement over SC_{BAT} because of the greater *NuSTAR* sensitivity. By contrast, only 2/10 well-known Compton-thick AGNs are found in the Compton-thick region based on the 8–24/3–8 keV ratio (Figure 5).

We compare the SC measurement from *NuSTAR* to the one we used with *Swift*/BAT for selection of the nine sources. The five sources with a *Swift*/BAT SC above the simulation upper limits for an edge-on torus (NGC 6232, CGCG 164-019, NGC

3393, MCG +06-16-028, UGC 3157) are now within the simulation results based on the *NuSTAR* SC. We find that 4/9 of the selected sources in our sample are firmly in the Compton-thick region at the 3σ level (NGC 3079, NGC 3393, MCG +06-16-028, 2MFGC 02280). Three fainter sources are just below the Compton-thick cutoff, but are consistent within errors of being Compton-thick (NGC 6232, NGC 7212 NED02, CGCG 164-019). Finally, NGC 3588 NED02 and UGC 3157 are below the cutoff at the 3σ level.

4.2. X-Ray Spectral Fitting

A plot of all the *NuSTAR* spectra before model fitting can be found in the top panel of Figure 7. We highlight the spectral features by showing the best-fit power-law model in the bottom two panels of Figure 7. Fitting the 3–10 keV *NuSTAR* spectra with a power-law model indicates $\Gamma < 1$ for all sources. This suggests that complex models are required. Additionally, a prominent excess is found at 6.4 keV, matching the Fe $K\alpha$ emission line. In order to measure the Fe $K\alpha$ equivalent width, we add a Gaussian component. We find a large equivalent width (>1 keV) for all nine sources. The high value of the equivalent width of the Fe $K\alpha$ lines is consistent with Compton-thick AGNs (e.g., Krolik & Kallman 1987; Levenson et al. 2002). At higher energies (>10 keV) an excess is seen between 10 and 25 keV for 8/9 AGNs; the remaining source, NGC 6232, shows an excess between 10 and 20 keV. The hard photon index ($\Gamma < 1$), high equivalent width fluorescent Fe $K\alpha$ lines, and Compton hump suggest a strong reflection component (e.g., Matt et al. 2000), which requires more complex models to accurately measure the column density.

4.2.1. Individual Torus Model Fits

We next self-consistently fit the X-ray absorption and scattering adopting a toroidal structure with fluorescent lines to derive the covering factor and torus inclination. A summary

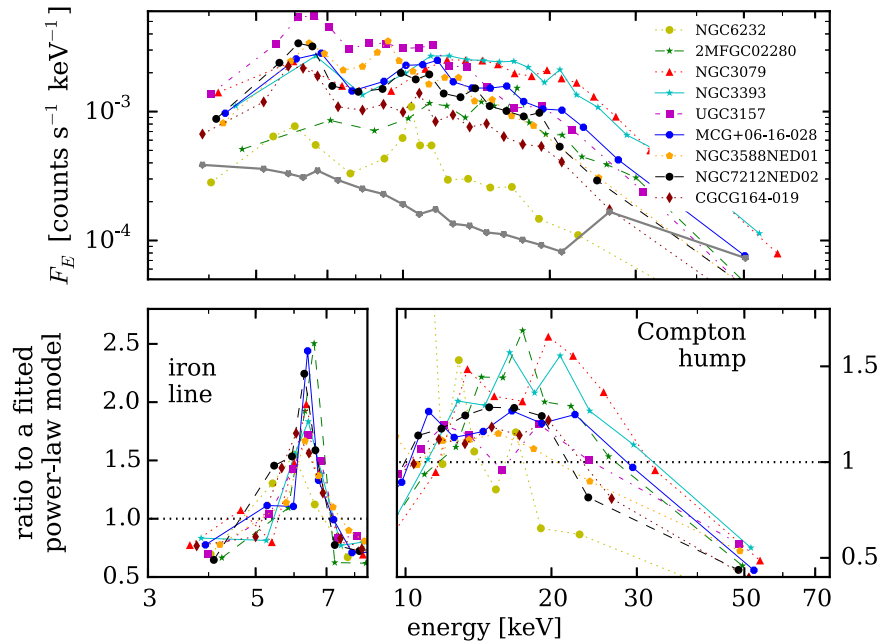


Figure 7. Top: observed *NuSTAR* spectra of nine galaxies selected based on their SC from *Swift*/BAT. Spectra for the two focal plane modules have been co-added. We have rebinned the spectra for each galaxy to have similar numbers of points in each panel at levels between 2.5σ (NGC 6232) and 15σ (NGC 3079). The typical background is shown by the filled gray symbols. Almost all sources are above the background level between 3 and 30 keV, except for NGC 6232, which is only above the background between 5 and 20 keV. Bottom left: ratio of the spectra and a simple power-law model fitted to the 3–10 keV spectra (symbols as in the panel above). We find that all sources show spectra consistent with a prominent Fe $K\alpha$ line (a decrement at 3–5 keV, an excess at 6–7 keV, and a decrement at 7–10 keV). Bottom right: ratio of the spectra and a simple power-law model fitted to the 10–70 keV spectra (symbols as in the panel above). We find that all sources show an excess at 10–25 keV, with the one exception, NGC 6232, showing an excess between 10 and 20 keV, where it is significantly detected.

of the best fits to the intrinsic absorbing column density (N_{H}), the intrinsic photon index (Γ), APEC model (kT), diffuse scattering component (f_{scatt}), and intrinsic X-ray luminosity (L_{X}) can be found in Table 3. Figure 8 shows the X-ray spectral fits with the best-fit torus-based model (Model M; described in Section 3.4) for the sample of nine *NuSTAR*-observed BAT AGNs. For Model T, none of our fits constrained the torus inclination angle, so we fix it here to edge-on ($\theta_{\text{inc}} = 85^\circ$). For the faintest source in our program, NGC 6232, Model M and Model T fits to the intrinsic absorbing column density (N_{H}) are poorly constrained, so we fix $\Gamma = 1.9$, $\theta_{\text{inc}} = 85^\circ$, and $\theta_{\text{tor}} = 60^\circ$, consistent with typical AGNs observed edge-on.

Our results confirm that the two brightest sources above 10 keV, NGC 3079 and NGC 3393, are Compton-thick in both Model M and Model T. This is in agreement with past studies with other X-ray telescopes (e.g., Iyomoto et al. 2001; Koss et al. 2015). Model M also suggests that the reflection/scattering component is dominant over the transmitted component. For both NGC 3079 and NGC 3393, the large-scale scattered component contributes the majority of the emission between 1 and 5 keV, with the APEC model dominant below 1 keV. For NGC 3079, the large scattering fraction ($f_{\text{scatt}} < 0.36$) may indicate additional soft components that are poorly fit. For NGC 7212 NED02, Model M suggests a Compton-thick source, whereas Model T suggests a source that is nearly Compton-thick ($N_{\text{H}} = 0.90^{+0.13}_{-0.09} \times 10^{24} \text{ cm}^{-2}$). For NGC 7212 NED02, Model M yields a better fit in terms of χ^2/dof , and the difference in column with Model T is likely associated with the strength of the large-scale diffuse scattered component, which is dominant below 3 keV and better fit with Model M. Finally, 2MFGC 02280 was also found to be Compton-thick by both Model M and Model T, consistent with an earlier *NuSTAR* study (Brightman et al. 2015).

2MFGC 02280 does not have a detection below 3 keV in *Swift*/XRT and lies in a high Galactic column region ($N_{\text{H}} = 4 \times 10^{21} \text{ cm}^{-2}$), so there are almost no constraints on the APEC model or diffuse scattering.

CGCG 164-019, MCG +06-16-028, and NGC 6232 also have model fits suggestive of being Compton-thick. Both Model M and Model T suggest Compton-thick levels of obscuration for MCG +06-16-028 and NGC 6232, with relatively large uncertainties in the column density and weak constraints on the APEC model and diffuse component. We note that for NGC 6232, the spectral index was fixed at $\Gamma = 1.9$ and the source may not be Compton-thick if $\Gamma < 1.7$. CGCG 164-019, like NGC 7212 NED02, has Model M suggesting a Compton-thick source, whereas Model T suggests a source that is only heavily obscured ($N_{\text{H}} = 0.55^{+0.24}_{-0.43} \times 10^{24} \text{ cm}^{-2}$). Some of the differences in column can be attributed to the higher Γ in Model M ($\Gamma = 2.0^{+0.3}_{-0.0}$) than Model T ($\Gamma = 1.6^{+0.3}_{-0.2}$). Both Model M and Model T yield similar χ^2 , so it is difficult to say more. Again the five detected counts below 3 keV in the *Swift*/XRT observations limit how well we can constrain the models.

The sources NGC 3588 NED02 and UGC 3157 have fits suggesting they are Compton-thin but heavily obscured ($N_{\text{H}} \approx 5 \times 10^{23} \text{ cm}^{-2}$) despite large Fe $K\alpha$ equivalent widths (>1 keV). Past studies have noted, however, that dusty Compton-thin gas can boost the Fe $K\alpha$ equivalent widths (Gohil & Ballantyne 2015). *Swift*/XRT detects no counts below 3 keV in NGC 3588 NED02 and only 4 counts in UGC 3157, limiting the model constraints. Finally, we note that a recently published compilation paper on Compton thick AGN in the BAT sample (Ricci et al. 2015) found broad agreement with our analysis (NGC 6232, NGC 7212 NED02, 2MFGC

Table 3
Best-fit Models for the *NuSTAR* + *Swift*/XRT Phenomenological versus Physically Motivated Torus Models

Object	Mod. ^a	χ^2/dof^b	Γ^c	N_{H}^d (10^{24} cm^{-2})	θ_{inc}^e ($^\circ$)	θ_{tor}^f ($^\circ$)	kT^g (keV)	$L_{2-10 \text{ keV}}^{\text{obs/int}^h}$ ($10^{41} \text{ erg s}^{-1}$)	$L_{14-50 \text{ keV}}^{\text{obs/int}^h}$ ($10^{41} \text{ erg s}^{-1}$)	f_{scatt}^i
2MFGC 02280	M	226/263	$2.1_{-0.1}^{+0.1}$	$3.16_{-0.30}^{+0.35}$	$70.8_{-4.63}^{+4.94}$	60	ND	0.8/204.6	20.5/113.7	ND
	T	228/264	$1.9_{-0.1}^{+0.0}$	$1.97_{-0.19}^{+0.71}$	85	$48.6_{-5.95}^{+10.5}$	ND	0.8/46.7	21.0/38.1	ND
CGCG 164-019	M	295/377	$2.0_{-0.1}^{+0.3}$	$3.02_{-0.86}^{+2.36}$	$61.3_{-0.95}^{+0.51}$	60	$0.5_{-0.5}^{+1.4}$	5.9/57.7	43.7/43.0	$0.01_{-0.01}^{+0.00}$
	T	303/378	$1.6_{-0.2}^{+0.3}$	$0.55_{-0.43}^{+0.24}$	85	$51.3_{-25.3}^{+31.1}$	$0.1_{-0.1}^{+0.4}$	6.1/30.2	41.7/46.8	$0.05_{-0.05}^{+0.00}$
MCG +06-16-028	M	465/566	$1.7_{-0.0}^{+0.3}$	$1.71_{-1.11}^{+4.59}$	$67.9_{-7.94}^{+17.6}$	60	$0.3_{-0.3}^{+0.4}$	2.2/45.3	29.2/55.0	ND
	T	469/567	$1.8_{-0.2}^{+0.3}$	$1.21_{-0.25}^{+0.26}$	85	$62.3_{-16.5}^{+19.3}$	$0.1_{-0.0}^{+0.1}$	2.2/49.3	28.6/46.6	ND
NGC 3079	M	543/287	$1.7_{-0.0}^{+0.0}$	$2.45_{-0.11}^{+0.23}$	$88.3_{-28.3}^{+1.61}$	60	$0.8_{-0.0}^{+0.0}$	0.1/R ^j	4.6/R	$0.36_{-0.36}^{+0.00}$
	T	534/288	$1.4_{-0.0}^{+0.1}$	$1.84_{-0.35}^{+0.28}$	85	$77.9_{-7.16}^{+3.72}$	$0.8_{-0.0}^{+0.0}$	0.1/5.8	4.2/12.2	ND
NGC 3393	M	1175/852	$1.8_{-0.1}^{+0.1}$	$2.06_{-0.33}^{+0.24}$	$87.9_{-27.9}^{+2.01}$	60	$0.3_{-0.0}^{+0.0}$	1.3/R	38.0/R	$0.04_{-0.04}^{+0.00}$
	T	1197/853	$2.1_{-0.0}^{+0.1}$	$2.16_{-0.01}^{+0.32}$	85	$26.0_{-7.30}^{+7.00}$	$0.2_{-0.0}^{+0.0}$	1.4/80.6	32.1/47.2	ND
NGC3588NED01	M	386/483	$1.7_{-0.0}^{+0.0}$	$0.60_{-0.03}^{+0.07}$	$89.3_{-10.4}^{+0.61}$	60	ND	7.3/75.1	51.7/94.5	ND
	T	385/484	$1.8_{-0.1}^{+0.0}$	$0.57_{-0.03}^{+0.05}$	85	$77.9_{-4.99}^{+6.02}$	ND	7.4/67.2	51.9/75.2	ND
NGC 6232	M	139/176	1.9	$1.23_{-0.23}^{+0.97}$	85	60	$0.4_{-0.4}^{+0.6}$	0.4/10.6	4.9/10.0	$0.01_{-0.01}^{+0.00}$
	T	144/176	1.9	$3.31_{-1.31}^{+5.39}$	85	60	$0.1_{-0.1}^{+1.8}$	0.5/22.6	6.8/21.3	$0.01_{-0.01}^{+0.00}$
NGC 7212 NED02	M	174/135	$1.9_{-0.0}^{+0.1}$	$2.64_{-0.45}^{+0.46}$	$61.1_{-0.15}^{+0.15}$	60	$0.8_{-0.0}^{+0.0}$	9.0/R	76.2/R	$0.02_{-0.02}^{+0.00}$
	T	227/136	$2.0_{-0.1}^{+0.2}$	$0.90_{-0.09}^{+0.13}$	85	$45.5_{-6.65}^{+31.3}$	$0.8_{-0.1}^{+0.0}$	8.9/119.0	70.2/89.6	$0.01_{-0.01}^{+0.00}$
UGC 3157	M	452/564	$1.7_{-0.0}^{+0.3}$	$0.57_{-0.18}^{+1.21}$	$87.0_{-27.0}^{+3.0}$	60	$0.0_{-0.0}^{+1.9}$	4.6/26.8	23.8/33.2	$0.01_{-0.01}^{+0.00}$
	T	454/565	$1.8_{-0.2}^{+0.0}$	$0.55_{-0.13}^{+0.09}$	85	$59.9_{-22.9}^{+24.0}$	$0.0_{-0.0}^{+1.9}$	4.6/25.9	23.9/28.7	ND

Notes. Best-fitting model parameters for the 0.5–70 keV spectrum. Parameters without errors have been fixed. The models are detailed in Section 3.4. The errors correspond to 90% confidence level for a single parameter. ND refers to model components that are not detected.

^a M—MYTORUS ; T—BNTORUS model.

^b The sources with *XMM-Newton* data, NGC7212 NED02 and NGC 3079, were binned to 20 counts per bin using χ^2 statistics, and the remaining sources were binned to 3 counts per bin using Poisson statistics.

^c The power-law photon index of the direct and scattered component.

^d Column density for the direct component. In the MYTORUS models the column density is equatorial rather than line of sight; however, for torus $\theta_{\text{inc}} > 60^\circ$ (which all the MYTORUS models converge to here) the difference between the equatorial and line-of-sight column density is less than 3%.

^e Best-fitting torus inclination angle to the observer.

^f Best-fitting torus opening angle. The MYTORUS model assumes a 60° opening angle.

^g Temperature of the best-fitting APEC component. A nondetection is listed when the 90% confidence upper limit is less than 0.01 keV.

^h Observed compared to intrinsic emission.

ⁱ Scattered fraction normalized to the intrinsic direct component. A nondetection is listed when the 90% confidence upper limit is less than a fraction of 0.01.

^j The intrinsic luminosity cannot be estimated because the source is reflection dominated (reflected/transmitted > 5) and the transmitted component is not detected.

02280, NGC 3079, NGC 3393, and MCG +06-16-028 were Compton-thick).

4.2.2. Summary of X-Ray Fits

In general, the Model M and Model T fits provide similar quality of fit χ^2/dof to the data with no systematic trend toward higher column density or power-law index for either model. We also report some overall properties from the SC-selected sample using the results from Model M and Model T. The mean power-law index is $\Gamma = 1.88 \pm 0.07$. The mean column is $N_{\text{H}} = (1.93 \pm 0.38) \times 10^{24} \text{ cm}^{-2}$. We find that the mean observed-to-intrinsic luminosity at 2–10 keV and 14–50 keV is $L_{2-10 \text{ keV}}^{\text{obs/int}} = 0.05 \pm 0.02$ and $L_{14-50 \text{ keV}}^{\text{obs/int}} = 0.59 \pm 0.08$, respectively. For this calculation, we used the Model T observed-to-intrinsic luminosity estimates for the reflection-dominated sources as determined from Model M. The torus inclination is found to have values between 60° and 90° (edge-on), while the torus half opening angle spans 26° – 78° .

Interestingly, our individual spectral fits broadly agree with our Compton-thick selection based on SC. Using SC, we found that NGC 3079, NGC 3393, MCG +06-16-028, and 2MFGC 02280 were all Compton-thick. The three fainter sources that lie just below the Compton-thick cutoff but within 1σ error of

being Compton-thick are all sources that might be Compton-thin using Model T. NGC 3588 NED02 and UGC 3157 are the only two sources significantly below the SC Compton-thick cutoff and are also Compton-thin when fitting the spectra.

Finally, we tried fitting a so-called MYTORUS “decoupled” model, where the N_{H} of the MYTS and MYTL components are allowed to vary compared to the zeroth-order transmitted continuum. In this “decoupled” model, the geometry can be thought of as a patchy torus where the global column density experienced by the scattered/reflection and fluorescent emission is different from the line-of-sight column density. However, we found that the quality of fit was not significantly better for any of the sources and the two-component N_{H} was poorly constrained given the quality of the data.

In summary, we find that torus models suggest that Compton-thick column densities are preferred for most (78% or 7/9) of the sources selected based on their SC values, with the remaining two sources being heavily obscured ($N_{\text{H}} > 5 \times 10^{23} \text{ cm}^{-2}$). We note that our study is limited in that 6/9 sources have low-quality *Swift*/XRT or *Chandra* data with only a handful of counts below 3 keV. Higher-quality spectroscopy would be required to place stronger constraints on the large scattered component, which may affect the column density measurements. While much brighter Compton-thick AGNs such as NGC 1068 exhibit additional complexities and

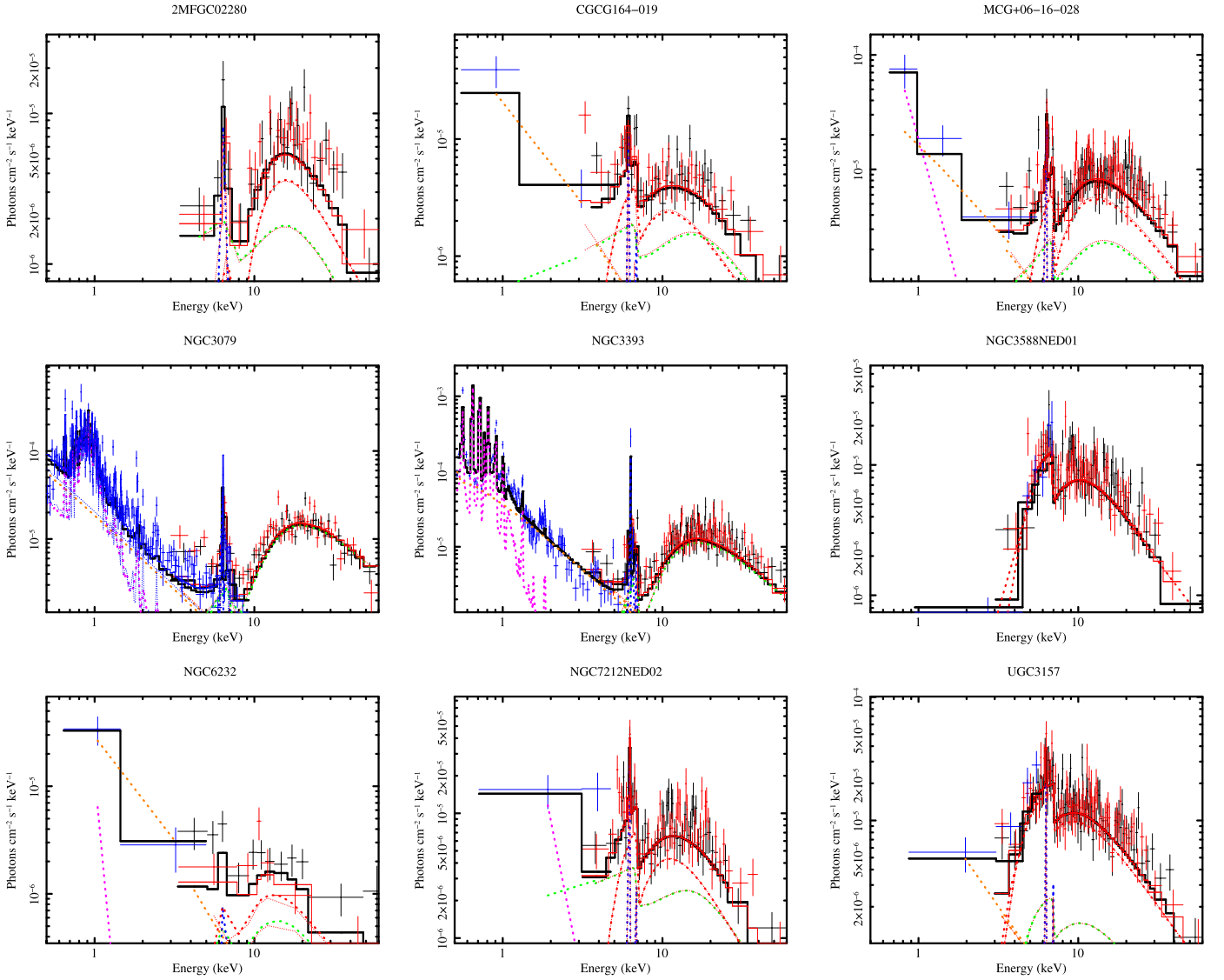


Figure 8. X-ray spectra of the nine *NuSTAR*-observed *Swift*/BAT AGNs selected based on SC. The best-fit MYTORUS-based model (MODEL M; described in Section 3.4) is shown binned to match the unfolded data. *NuSTAR* is shown in black (FPMA) and red (FPMB) crosses, while blue crosses represent the soft X-ray data. The soft X-ray data are from *XMM-Newton* for NGC 3079 and NGC 7212 NED02, *Chandra* for NGC 3393 and NGC 3588 NED02, and *Swift*/XRT for the remaining sources. The data are shown grouped to a minimum significance of 3.5σ per bin for visual purposes. The sum of the model is represented by a solid black line. The model components are represented by dashed lines indicating the zeroth-order transmitted continuum through photoelectric absorption (MYTZ, red), the scattered/reflected component (MYTS, green), and fluorescent emission-line spectrum (MYTL, dark blue). At softer energies (<3 keV), there is a model component for scattered AGN emission on larger scales in the host galaxy (f_{scatt} , orange) and in some models there is a thermal plasma component (APEC, pink).

Table 4
Compton-thick AGN Indicators

Object	Fe $K\alpha$ EW > 1 keV	Γ < 1	<i>NuSTAR</i> SC	MYTORUS Model	$F_{2-10 \text{ keV}}^{\text{obs}}/F_{2-10 \text{ keV}}^{\text{pred } 6 \mu\text{m}}$ < 20	IR SED $E(B - V)$	$F_{2-10 \text{ keV}}^{\text{obs}}/F_{(0.1 \text{ m})}$ < 1
2MFGC 02280	T	T	T	T	T	T	N
CGCG 164-019	T	T	T	T	T	N	N
MCG +06-16-028	T	T	T	T	T	N	N
NGC 3079	T	T	T	T	T	N	T
NGC 3393	T	T	T	T	T	T	T
NGC 3588 NED02	T	T	N	N	N	T	N
NGC 6232	T	T	N	T	T	N	N
NGC 7212 NED02	T	T	N	T	T	T	...
UGC 3157	T	T	N	N	T	T	N

Note. Results of various tests of Compton thickness. N indicates that the object is Compton-thin, T indicates that the object was classified as Compton-thick, and an ellipse indicates that the test could not be performed on the object because of a lack of data.

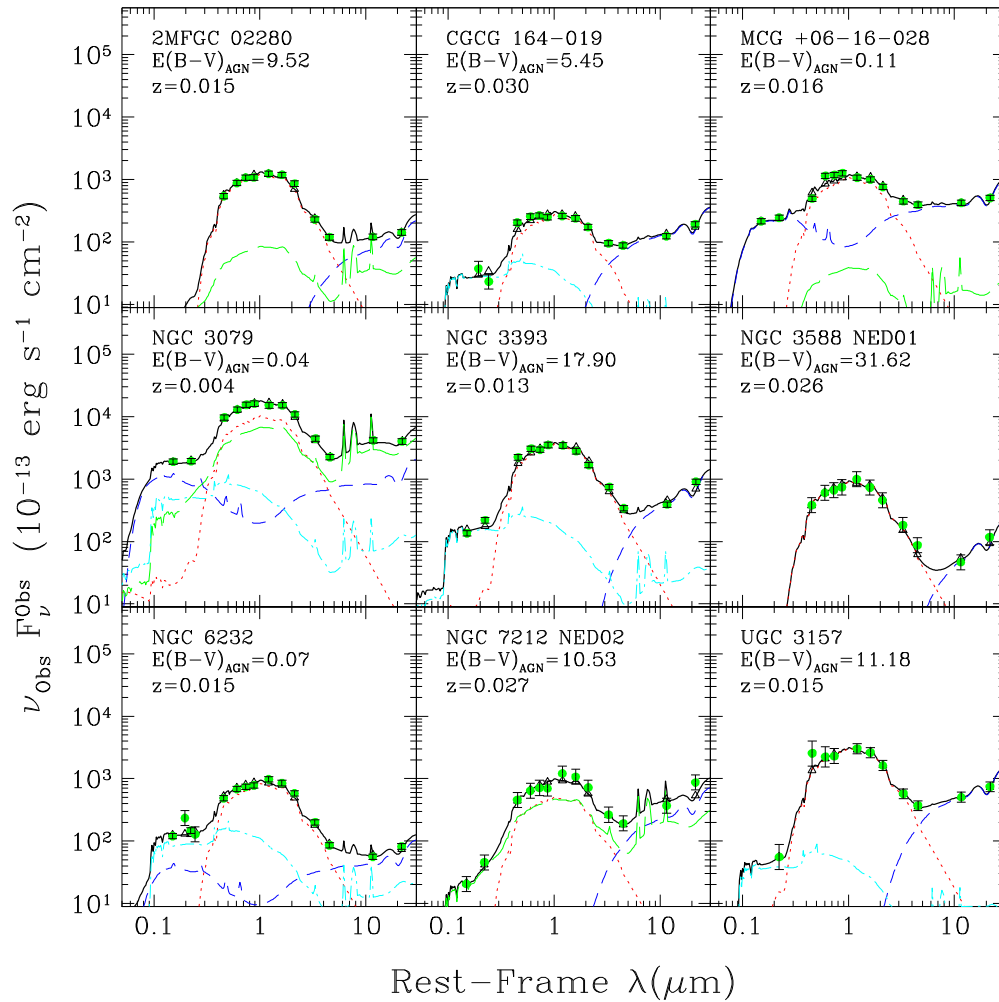


Figure 9. SEDs of the nine SC-selected galaxies. The observed photometry includes optical (*griz*), NIR (*JHK*), and mid-IR (3.4–22 μm), as well as FUV and NUV photometry when available. We used the Assef et al. (2010) 0.03–30 μm algorithm to model the strength of the AGN emission in the IR using empirical AGN and galaxy templates. The plot points represent observed data (green circles) and predicted SED model flux (open triangles). The total best-fit SED template line (solid black) was made by combining the AGNs (dashed blue) and old (E, dashed red), intermediate (Sbc, dashed green), and young (Im, dashed cyan) galaxy stellar populations.

components that are important to model (e.g., Bauer et al. 2014), testing for these is currently not possible because of the faintness of these sources and the comparatively low photon statistics from the short, ≈ 20 ks observations.

4.3. Other Measures of Compton Thickness

Another way to identify Compton-thick AGNs is to use additional intrinsic luminosity indicators (e.g., $L_{6\mu\text{m}}$, $L_{[\text{O III}]}$) to compare to the observed X-ray luminosity. A high mid-IR/X-ray ratio and/or high $[\text{O III}]/\text{X-ray}$ ratio may indicate a Compton-thick AGN. A summary of all the indicators including the results from the X-rays is provided in Table 4.

4.3.1. IR Emission

The 6 μm AGN emission provides an additional assessment of the intrinsic AGN luminosity (e.g., Gandhi et al. 2009). Moderate-luminosity AGNs, however, can have the majority of their mid-IR emission from host galaxy contributions (e.g., Stern et al. 2012) rather than the AGN. We therefore first measure the *WISE* colors to test whether the sources show colors indicative of AGNs and are dominated by AGN

emission in the mid-IR. We find that only three sources have $W1 - W2 > 0.8$, indicating that the AGN likely dominates the mid-IR emission (MCG +06-16-028, CGCG 164-019, and NGC 7212 NED02). It is therefore important to fit the spectral energy distributions (SEDs) to measure the intrinsic 6 μm AGN emission. The observed photometry includes optical (*griz* from Koss et al. 2011b), near-infrared (NIR; Two Micron All Sky Survey [2MASS] *JHK*), mid-IR (*WISE*, 3.4–22 μm), and *GALEX* or *Swift* far-ultraviolet and near-ultraviolet photometry when available. We follow the photometry procedure of Koss et al. (2011b) using Kitt Peak or 2MASS data to measure the optical and NIR photometry. We use the Assef et al. (2010) 0.03–30 μm algorithm to model the strength of the AGN emission in the mid-IR using empirical AGN and galaxy templates. The template SEDs (Figure 9) suggest a Compton-thick level of obscuration for most of the sample (5/9, 55%) based on the $N_{\text{H}}/E(B - V) = 1.5 \times 10^{23} \text{ cm}^{-2}$ conversion from reddening to column density (Maiolino et al. 2001).

For NGC 3079, MCG +06-16-028, and NGC 6232, almost no obscuration is detected ($E[B - V] < 0.11$) in the best-fit SEDs. This is inconsistent with the X-ray spectral fitting and the lack of broad lines in the optical spectra. To understand the

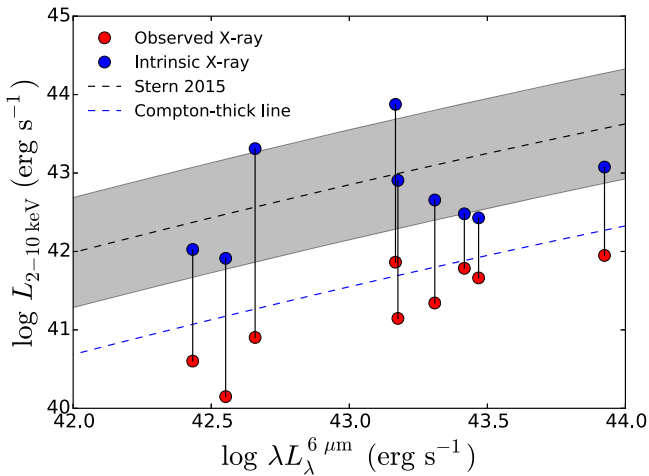


Figure 10. $L_{6\ \mu\text{m}}$ from SED fitting compared to $L_{2-10\ \text{keV}}^{\text{obs}}$ (red dot) and $L_{2-10\ \text{keV}}$ (blue dot) based on X-ray model fitting. A black dashed line indicates the relation from Stern (2015), and a gray region has been shaded within a factor of five of the mean ratio (± 0.7 dex). Sources below the blue dashed line are likely to be Compton-thick. All the sources except for NGC 3588 NED02 are below the Compton-thick line based on their mid-IR to observed X-ray emission. Finally, we find that even with the X-ray spectral fitting, the majority of the intrinsic estimates of the source luminosity are below the values expected from the $L_{6\ \mu\text{m}}$, suggesting that they may still be underestimated.

fitting better, we produced 1000 resampled SEDs based on the measured photometry but resampled by the photometric errors (assuming Gaussian noise) and find that the SED fits do include a small percentage of solutions with Compton-thick obscuration ($< 5\%$). The high AGN obscuration ($N_{\text{H}} > 10^{24}\ \text{cm}^{-2}$), combined with significant host galaxy star formation as shown by the bright UV and IR emission as seen in *Herschel* (Meléndez et al. 2014), makes SED techniques unable to accurately model the AGN SED in some cases due to the lack of photometric bands where the AGN is dominant. Further mid-IR studies using high spatial resolution imaging of nuclear emission (e.g., Asmus:2014:1648; Asmus et al. 2014) are required to resolve these degeneracies.

We estimate the intrinsic $6\ \mu\text{m}$ AGN emission from the template fitting and compare it to the observed 2–10 keV X-ray emission. We compare it to the ratio obtained from large-sample studies of AGNs (Stern 2015). This ratio is luminosity dependent, with a predicted X-ray to mid-IR ratio from 0.87 for our least luminous mid-IR source (NGC 6232) to 0.44 for the most luminous mid-IR source (NGC 7212 NED02). Assuming Model M and $\Gamma = 1.9$, the observed 2–10 keV X-ray emission is diminished by a factor of ≈ 20 at Compton-thick obscuration. We find that the observed X-ray emission is fainter than expected from the mid-IR (Figure 10) in all our sources by an average factor of 72 ± 29 . The smallest difference is NGC 3588 NED02 (factor of 13 lower X-ray emission), and the largest difference is NGC 3079 (factor of 298 lower). NGC 3588 NED02 is also the only AGN whose mid-IR to X-ray ratio ($L_{2-10\ \text{keV}}^{\text{obs}}/L_{6\ \mu\text{m}}$) is consistent with a Compton-thin AGN. Thus, the intrinsic mid-IR AGN emission confirms that the observed X-ray emission is consistent with Compton-thick AGNs for most of the sample.

4.3.2. Optical Spectroscopy

We compare the optical spectroscopy of these sources with other BAT-detected AGNs (Koss et al. 2016, in preparation).

We have optical spectra for all sources except NGC 7212 NED02. We first apply AGN emission-line diagnostics (e.g., Veilleux & Osterbrock 1987; Kewley et al. 2006) using the $[\text{N II}]/\text{H}\alpha$ diagnostic. All the AGNs are in the Seyfert or LINER region, except NGC 3588 NED02, which falls in the composite region, but this has been found with many other AGNs in close mergers (e.g., Koss et al. 2011a). The $\text{H}\beta$ line for 2MFGC 02280 is not detected, but the limit places it most likely in the Seyfert or LINER region. The ratio of the observed 2–10 keV X-ray to Balmer decrement corrected $[\text{O III}]$ line strength provides a measure of Compton thickness (Bassani et al. 1999). We find that only NGC 3393 and NGC 3079 show an excess in the Balmer decrement corrected $[\text{O III}]$ versus X-ray luminosity ratio consistent with a Compton-thick AGN ($F_{2-10\ \text{keV}}^{\text{obs}}/F_{[\text{O III}]} < 1$).

AGNs are known to have a wide range in $[\text{O III}]$ to X-ray ratios. One possibility for the low values of $[\text{O III}]$ is a low scattering fraction from a “buried” AGN (Ueda et al. 2007) with a small opening angle and/or having an unusually small amount of gas responsible for scattering. Additionally, if these AGNs have high Eddington ratios, they should have relatively weak $[\text{O III}]$ as found by the “Eigenvector 1” relationships (e.g., Boroson & Green 1992). Finally, AGN “flickering” on shorter timescales than the light-travel time to the ionized regions can cause some AGNs to have much stronger X-ray emission since it has just begun to ionize the narrow-line region (Schawinski et al. 2015). Noguchi et al. (2010) found that optical emission-line studies are biased against “buried” AGNs that have a small scattering fraction or a small amount of narrow-line region gas. AGNs with a low ratio of $[\text{O III}]$ to X-ray luminosity ($L_{[\text{O III}]} / L_{2-10\ \text{keV}}$) tend to be “buried” AGNs. We use the estimated ratio obtained from large studies of AGNs (Berney et al. 2015). In our sample, we find that only 2MFGC 02280 is consistent with a “buried” AGN in that the X-ray emission is significantly outside the scatter of the mean $[\text{O III}]$ to X-ray ratio ($L_{[\text{O III}]} / L_{14-195\ \text{keV}}^{\text{obs}}$). NGC 3588 NED02 does have a higher X-ray to $[\text{O III}]$ ratio, but this ratio has been found to be elevated in many merging AGN galaxies (Koss et al. 2010). In summary, the majority of the sample does not show evidence of having uniquely high intrinsic X-ray to $[\text{O III}]$ values.

4.4. Host Morphology and Accretion Rates

We investigate whether our sources have unique host morphologies or accretion rates compared to the rest of the nearby BAT AGN. Tricolor *gri* filter images for the nine sources selected based on *Swift*/BAT SC are shown in Figure 11. We find that 22% (2/9) of the sample is in close mergers ($< 10\ \text{kpc}$). In both sources, faint tidal tails and radial velocity differences of less than $500\ \text{km s}^{-1}$ (from NED) between the sample galaxy and its possible companion suggest an ongoing major merger rather than a chance association. NGC 3588 NED02 has a separation of 4.2 kpc ($8''.1$). NGC 7212 NED02 is in a galaxy triple with a separation of 9.8 kpc ($18''.3$) from NGC 7212 NED03 and a separation of 22 kpc ($41''.7$) from NGC 7212 NED01. This fraction is higher than typically found for BAT AGNs; Koss et al. (2010) found that 8% (11/144) of BAT AGNs are in close mergers ($< 10\ \text{kpc}$), though consistent within Poisson errors. With such a small sample size, this difference is not significant based on a Fisher exact test.

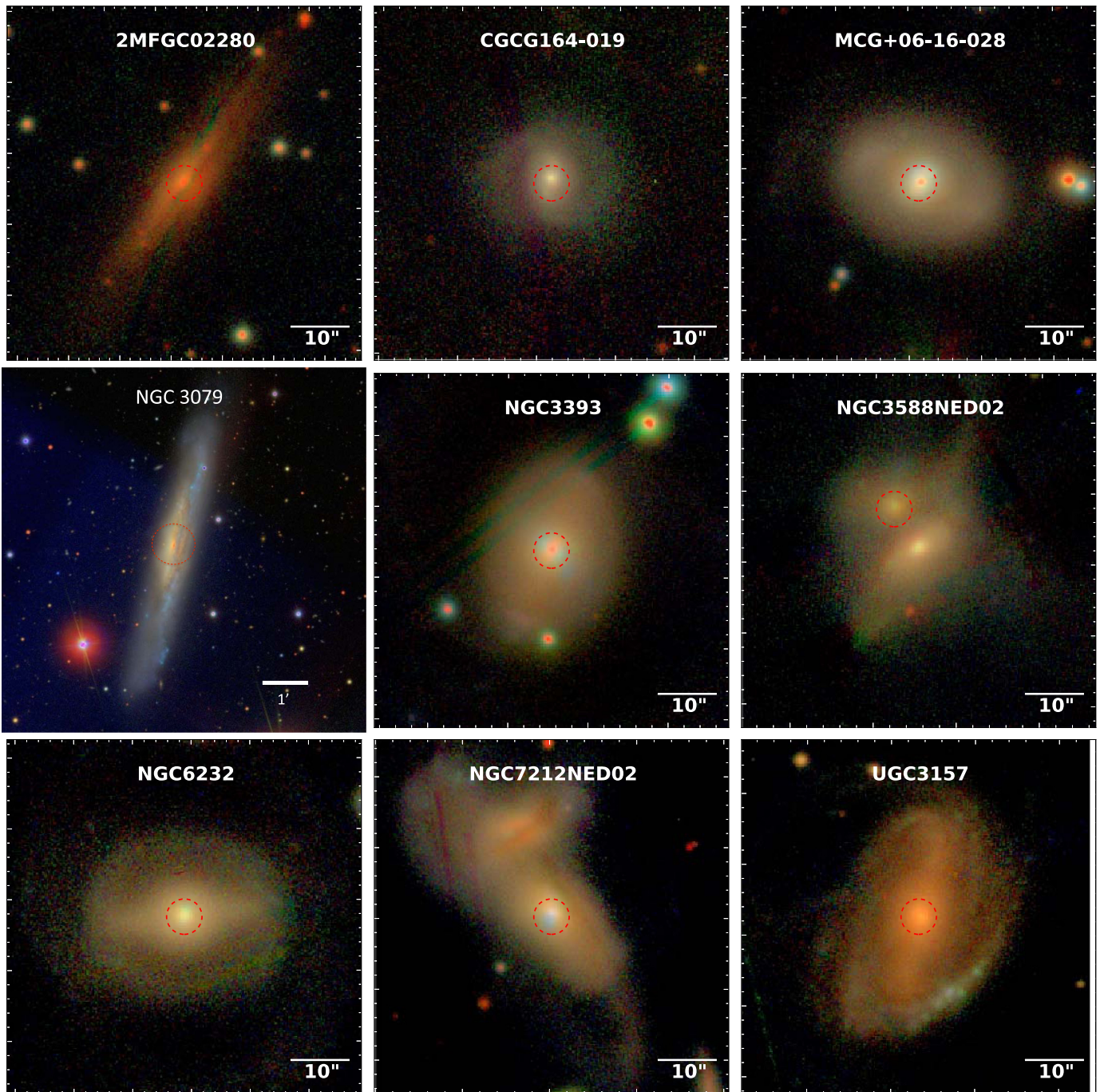


Figure 11. Tricolor optical images in *gri* displayed with an arcsinh scale for nine sources selected based on *Swift*/BAT SC. Images are $1'$ on a side except for NGC 3079, which is $8'$ on a side. A red dashed circle indicates the BAT-detected counterpart based on soft X-ray data from *Swift*/XRT. For NGC 3588 NED02 and NGC 7212 NED02, *Chandra* data confirm that the majority of the hard X-ray emission is coming from the galaxy nucleus and not the merging counterpart ($>95\%$ at 2–8 keV). The high fraction of sources in close (<10 kpc) mergers (22%, 2/9) and/or highly edge-on ($b/a < 0.22$) galaxies (22%, 2/9) suggests a possible connection of high levels of obscuration to the final merger stage and host galaxy inclination.

To investigate this further, we use the Koss et al. (2010) study, which had high-quality imaging and optical spectroscopy to study the companion separation. We find that the other two *NuSTAR*-observed AGNs in close mergers, NGC 6240 and 2MASX J00253292+6821442, are also in the SC Compton-thick regime ($SC_{\text{NuSTAR}} = 0.49 \pm 0.01$ and $SC_{\text{NuSTAR}} = 0.56 \pm 0.05$; NGC 6240 and 2MASX J00253292+6821442). The likelihood of finding all four sources being Compton-thick is $<1\%$ based on a Fisher test.

Another interesting morphological feature is that 22% (2/9) of the galaxies from the program (NGC 3079 and 2MFGC 02280) are nearly edge-on. Koss et al. (2011b) derived the axis ratio (b/a) from the major and minor axes derived from isophotal *r*-band photometry for both of these galaxies (NGC 3079; $b/a = 0.15$ and 2MFGC 02280; $b/a = 0.21$). By comparison, 6% of BAT AGNs have $b/a < 0.22$ (Koss et al. 2011b). The frequency of edge-on galaxies selected using SC versus the other BAT AGNs is not statistically significant

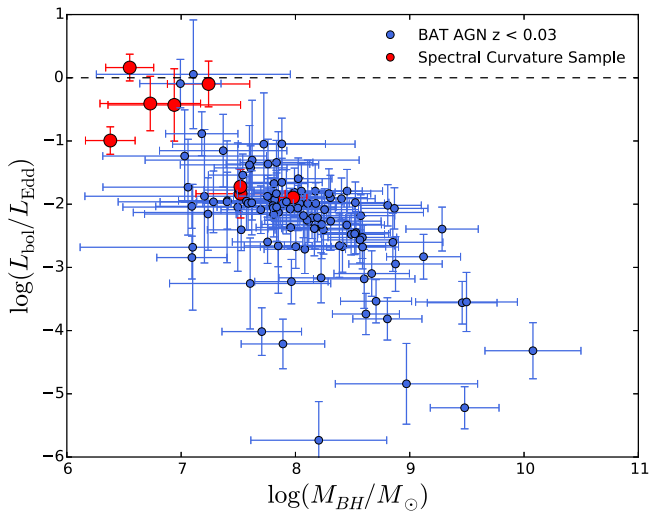


Figure 12. Eddington ratio of our heavily obscured AGNs compared to other nearby ($z < 0.03$) BAT-detected AGNs. We find that these sources typically are in the upper left quadrant of the sample with higher accretion rates and smaller black holes than typical BAT-detected AGNs.

because of the small sample size based on a Fisher test (11% chance), implying that larger samples are needed.

We compare the black hole mass and Eddington ratio of our sources to the other nearby BAT-detected AGNs. We use the velocity dispersion measurements for measurements of black hole mass (from Koss et al. 2016, in preparation) and the median and median absolute deviation (MAD) to compare the populations because of the spread over several orders of magnitude. We find that the typical black hole mass of our sample is a factor of four smaller than typical BAT-detected AGNs ($M_{\text{BH}} = (1.3 \pm 0.4) \times 10^7 M_{\odot}$ versus $M_{\text{BH}} = (5.1 \pm 0.4) \times 10^7 M_{\odot}$), where the error refers to the MAD 1σ error.

We also estimated the bolometric luminosity L_{bol} from the X-ray luminosity ($L_{14-195 \text{ keV}}^{\text{obs}}$) using the bolometric corrections from Vasudevan & Fabian (2009). Including the absorption-corrected 14–195 keV emission based on the *NuSTAR* spectral fitting of our sources, the typical Eddington ratio of our sources is about a factor of four larger ($\lambda_{\text{Edd}} = 0.068 \pm 0.023$ compared to $\lambda_{\text{Edd}} = 0.016 \pm 0.004$), where the error refers to the 1σ error in the MAD (Figure 12). A Kolmogorov–Smirnov test indicates a $< 1\%$ chance that the distribution of Eddington ratios for SC-selected BAT AGNs is from the same parent distribution as the other BAT AGNs. This indicates that the SC-selected BAT AGNs have, on average, higher accretion rates.

5. SUMMARY

We define a new SC measure of Compton thickness using weighted averages of different energy bands in the low-sensitivity *Swift*/BAT survey. We then select nine AGNs for *NuSTAR* follow-up to study their possible Compton-thick nature.

- i. We find that all nine targeted sources are consistent with Compton-thick AGNs in the majority of indicators (e.g., Fe $K\alpha$ EW > 1 keV, $\Gamma < 1$, X-ray spectra fitting, mid-IR indicators), confirming the effectiveness of the SC method to identify new Compton-thick AGNs. Using *NuSTAR* spectroscopy, the majority of the nine targets are consistent with Compton-thick AGNs using

MYTORUS models (78%, 7/9), and the remaining two are nearly Compton-thick ($N_{\text{H}} \simeq (5-8) \times 10^{23} \text{ cm}^{-2}$). The observed 2–10 keV emission compared to the $6 \mu\text{m}$ emission is also consistent with a Compton-thick AGN for most sources (8/9, 89%; $F_{2-10 \text{ keV}}^{\text{obs}}/F_{2-10 \text{ keV}}^{\text{pred } 6 \mu\text{m}} > 20$).

- ii. Our results suggest that the > 10 keV emission may be the only way to identify this population of Compton-thick AGNs other than through detailed SED fitting. We find that only two sources show evidence of an excess in the Balmer decrement corrected [O III] versus X-ray luminosity consistent with a Compton-thick AGN ($F_{[\text{O III}]}/F_{2-10 \text{ keV}}^{\text{obs}} > 1$). As expected for lower-luminosity AGNs, we find that most sources (6/9, 67%) would not be identified as AGNs using *WISE* colors, though detailed SED fitting with the mid-IR would identify most sources.
- iii. We find the SC_{BAT} and $\text{SC}_{\text{NuSTAR}}$ measurements to be consistent on average ($\text{SC}_{\text{BAT}} = 0.29 \pm 0.07$ vs. $\text{SC}_{\text{NuSTAR}} = 0.27 \pm 0.03$). This suggests that this measure can be used with other satellites with > 10 keV coverage such as *Astro-H*, or high-redshift AGNs ($z > 3$) observed with *Chandra* or *Athena*, where the bands are shifted to cover rest frame 10–30 keV.
- iv. We find that the SC measure is much more effective at selecting Compton-thick AGNs than band ratios (8–24 keV/3–8 keV), finding 10/10 well-known Compton-thick AGNs compared to only 2/10 using band ratios.
- v. We find that these heavily obscured AGNs have smaller black holes ($\langle M_{\text{BH}} \rangle = (1.3 \pm 0.36) \times 10^7 M_{\odot}$ vs. $\langle M_{\text{BH}} \rangle = (5.1 \pm 0.39) \times 10^7 M_{\odot}$) and higher accretion rates than other BAT-detected AGNs ($\langle \lambda_{\text{Edd}} \rangle = 0.068 \pm 0.023$ compared to $\langle \lambda_{\text{Edd}} \rangle = 0.016 \pm 0.004$).

We find that the four *NuSTAR*-observed sources in very close mergers (< 10 kpc) are all found to be Compton-thick, suggesting a physically plausible link between increased gas supply and obscuration, which might be natural in the early stages of a merger (e.g., Sanders et al. 1988; Hopkins et al. 2005). Based on simulations, the timescale within 10 kpc for major mergers is relatively short, on the order of 100–200 Myr (Van Wassenhove et al. 2012), so finding even a small number of galaxies may be significant. Another interesting morphological feature is that 2/9 program sources are in extremely edge-on galaxies ($b/a < 0.25$), suggesting that galaxy-wide extinction may be important for some sources. This compares to only 6% of BAT AGNs. The likelihood of this occurring by chance is 11%, implying that larger samples are needed.

Based on the robustness of SC in identifying Compton-thick AGNs, we measure the fraction of Compton-thick nearby BAT AGNs ($z < 0.03$) as $\approx 22\%$ ($\text{SC}_{\text{BAT}} = 22\%$, $\text{SC}_{\text{NuSTAR}} = 21\%$). The Compton-thick number density is $(2.3 \pm 0.3) \times 10^{-6} \text{ Mpc}^{-3}$ above $L_{2-10 \text{ keV}} > 10^{43} \text{ erg s}^{-1}$. This is a conservative estimate since *Swift*/BAT likely misses reflection-dominated AGNs. This number is significantly higher than previous work with *Swift*/BAT, which reported only a handful of Compton-thick AGNs corresponding to fractions of a few percent (e.g., Tueller et al. 2008; Winter et al. 2009; Burlon et al. 2011; Vasudevan et al. 2013). This 22% fraction is in line with estimates of the intrinsic Compton-thick fraction in X-ray background population-synthesis models (5%–52% of obscured AGNs; for review see Ueda et al. 2014).

These Compton-thick AGNs show high Eddington ratios consistent with other well-known Compton-thick AGNs in the BAT sample already observed with *NuSTAR* (e.g., Circinus, $\lambda_{\text{Edd}} = 0.2$; NGC 4945, $\lambda_{\text{Edd}} = 0.1\text{--}0.3$; NGC 1068, $\lambda_{\text{Edd}} = 0.5\text{--}0.8$ —Arévalo et al. 2014; Bauer et al. 2014; Puccetti et al. 2014) and also in recent results from the *XMM-COSMOS* survey (Lanzuisi et al. 2015b). This suggests that the sum of black hole growth in Compton-thick AGNs (Eddington ratio times population percentage) may be nearly as much as the rest of the population of mildly obscured AGNs and unobscured AGNs. A highly obscured ($N_{\text{H}} > 10^{24} \text{ cm}^{-2}$), high-Eddington population ($\lambda_{\text{Edd}} > 0.1$) like these AGNs could be important for resolving discrepancies based on considerations of the Soltan argument (e.g., Brandt & Alexander 2015; Comastri et al. 2015). Additionally, the high Eddington ratios with relatively weak [O III] to X-ray ratio, despite being Compton-thick, are consistent with the “Eigenvector 1” relationships (e.g., Boroson & Green 1992). In further studies, we will use much larger samples of BAT-detected AGNs with measured black hole masses and accretion rates to study which populations have most of the black hole growth (Koss et al. 2016, in preparation).

We acknowledge financial support from Ambizione fellowship grant PZ00P2_154799/1 (M.K.), the Swiss National Science Foundation (NSF) grant PP00P2 138979/1 (M.K. and K.S.), the Center of Excellence in Astrophysics and Associated Technologies (PFB 06), by the FONDECYT regular grant 1120061 and by the CONICYT Anillo project ACT1101 (E. T.), NASA Headquarters under the NASA Earth and Space Science Fellowship Program, grant NNX14AQ07H (M.B.), NSF award AST 1008067 (D.B.), Caltech *NuSTAR* subcontract 44A-1092750 and NASA ADP grant NNX10AC99G (W. N.B.), and the ASI/INAF grant I/037/12/0 011/13 and the Caltech Kingsley visitor program (A.C.). M.K. also acknowledges that support for this work was provided by the National Aeronautics and Space Administration through *Chandra* Award Number AR3-14010X issued by the *Chandra* X-ray Center, which is operated by the Smithsonian Astrophysical Observatory for and on behalf of the National Aeronautics Space Administration under contract NAS8-03060. This work was supported under NASA Contract No. NNG08FD60C and made use of data from the *NuSTAR* mission, a project led by the California Institute of Technology, managed by the Jet Propulsion Laboratory, and funded by the National Aeronautics and Space Administration. We thank the *NuSTAR* Operations, Software and Calibration teams for support with the execution and analysis of these observations. This research has made use of the *NuSTAR* Data Analysis Software (NuSTARDAS) jointly developed by the ASI Science Data Center (ASDC, Italy) and the California Institute of Technology (USA). This research made use of the XRT Data Analysis Software (XRTDAS), archival data, software, and online services provided by the ASDC. This work made use of data supplied by the UK Swift Science Data Centre at the University of Leicester. The scientific results reported in this article are based on data obtained from the *Chandra* Data Archive (Obs ID = 4078, 4868, 12290, 13895). This work is based on observations obtained with *XMM-Newton* (Obs ID = 0110930201, 0147760101, 0200430201), an ESA science mission with instruments and contributions directly funded by ESA Member States and NASA.

Facilities: NuSTAR, Swift, XMM, Sloan, CXO

REFERENCES

- Ajello, M., Alexander, D. M., Greiner, J., et al. 2012, *ApJ*, 749, 21
 Alexander, D. M., Chary, R. R., Pope, A., et al. 2008, *ApJ*, 687, 835
 Arévalo, P., Bauer, F. E., Puccetti, S., et al. 2014, *ApJ*, 791, 81
 Asmus, D., Hönig, S. F., Gandhi, P., Smette, A., & Duschl, W. J. 2014, *MNRAS*, 439, 1648
 Assef, R. J., Kochanek, C. S., Brodwin, M., et al. 2010, *ApJ*, 713, 970
 Baloković, M., Comastri, A., Harrison, F. A., et al. 2014, *ApJ*, 794, 111
 Baloković, M., Matt, G., Harrison, F. A., et al. 2015, *ApJ*, 800, 62
 Barthelmy, S. D., Barbier, L. M., Cummings, J. R., et al. 2005, *SSRv*, 120, 143
 Bassani, L., Dadina, M., Maiolino, R., et al. 1999, *ApJS*, 121, 473
 Bauer, F. E., Arévalo, P., Walton, D. J., et al. 2014, *ApJ*, 812, 116
 Baumgartner, W. H., Tueller, J., Markwardt, C. B., et al. 2013, *ApJS*, 207, 19
 Berney, S., Koss, M., Trakhtenbrot, B., et al. 2015, *MNRAS*, 454, 3622
 Boroson, T. A., & Green, R. F. 1992, *ApJS*, 80, 109
 Brandt, W. N., & Alexander, D. M. 2015, *A&ARv*, 23, 1
 Brightman, M., Baloković, M., Stern, D., et al. 2015, *ApJ*, 805, 41
 Brightman, M., & Nandra, K. 2011, *MNRAS*, 413, 1206
 Burlon, D., Ajello, M., Greiner, J., et al. 2011, *ApJ*, 728, 58
 Burrows, D. N., Hill, J. E., Nousek, J. A., et al. 2005, *SSRv*, 120, 165
 Cardamone, C. N., Urry, C. M., Damen, M., et al. 2008, *ApJ*, 680, 130
 Comastri, A., Gilli, R., Marconi, A., Risaliti, G., & Salvati, M. 2015, *A&A*, 574, L10
 Del Moro, A., Alexander, D. M., Mullaney, J. R., et al. 2013, *A&A*, 549, A59
 Donley, J. L., Koekemoer, A. M., Brusa, M., et al. 2012, *ApJ*, 748, 142
 Draper, A. R., & Ballantyne, D. R. 2010, *ApJL*, 715, L99
 Eckart, M. E., McGreer, I. D., Stern, D., Harrison, F. A., & Helfand, D. J. 2010, *ApJ*, 708, 584
 Evans, P. A., Beardmore, A. P., Page, K. L., et al. 2009, *MNRAS*, 397, 1177
 Gandhi, P., Horst, H., Smette, A., et al. 2009, *A&A*, 502, 457
 Gandhi, P., Lansbury, G. B., Alexander, D. M., et al. 2014, *ApJ*, 792, 117
 Gilli, R., Comastri, A., & Hasinger, G. 2007, *A&A*, 463, 79
 Gohil, R., & Ballantyne, D. R. 2015, *MNRAS*, 449, 1449
 Guainazzi, M., Matt, G., Antonelli, L. A., et al. 1999, *Monthly Notices*, 310, 10
 Harrison, F. A., Craig, W. W., Christensen, F. E., et al. 2013, *ApJ*, 770, 103
 Hernández-García, L., Masegosa, J., González-Martín, O., & Marquez, I. 2015, *A&A*, 579, A90
 Hopkins, P. F., Hernquist, L., Martini, P., et al. 2005, *ApJL*, 625, L71
 Iyamoto, N., Fukazawa, Y., Nakai, N., & Ishihara, Y. 2001, *ApJL*, 561, L69
 Keck, M. L., Brenneman, L. W., Ballantyne, D. R., et al. 2015, *ApJ*, 806, 149
 Kewley, L. J., Groves, B., Kauffmann, G., & Heckman, T. 2006, *MNRAS*, 372, 961
 Koss, M., et al. 2016, *ApJ*, submitted
 Koss, M., Mushotzky, R., Treister, E., et al. 2011a, *ApJL*, 735, L42
 Koss, M., Mushotzky, R., Treister, E., et al. 2012, *ApJL*, 746, L22
 Koss, M., Mushotzky, R., Veilleux, S., et al. 2011b, *ApJ*, 739, 57
 Koss, M., Mushotzky, R., Veilleux, S., & Winter, L. 2010, *ApJL*, 716, L125
 Koss, M. J., Romero-Cañizales, C., Baronchelli, L., et al. 2015, *ApJ*, 807, 149
 Krolik, J. H., & Kallman, T. R. 1987, *ApJL*, 320, L5
 Lanzuisi, G., Perna, M., Delvecchio, I., et al. 2015a, *A&A*, 578, A120
 Lanzuisi, G., Ranalli, P., Georgantopoulos, I., et al. 2015b, *A&A*, 573, A137
 Levenson, N. A., Krolik, J. H., Życki, P. T., et al. 2002, *ApJL*, 573, L81
 Levine, A. M., Lang, F. L., Lewin, W. H. G., et al. 1984, *ApJS*, 54, 581
 Luo, B., Brandt, W. N., Xue, Y. Q., et al. 2011, *ApJ*, 740, 37
 Madsen, K. K., Harrison, F. A., Markwardt, C., et al. 2015, *ApJS*, 220, 8
 Maiolino, R., Marconi, A., Salvati, M., et al. 2001, *A&A*, 365, 28
 Matt, G., Fabian, A. C., Guainazzi, M., et al. 2000, *MNRAS*, 318, 173
 Meléndez, M., Mushotzky, R. F., Shimizu, T. T., Barger, A. J., & Cowie, L. L. 2014, *ApJ*, 794, 152
 Miller, L., Peacock, J. A., & Mead, A. R. G. 1990, *MNRAS*, 244, 207
 Murphy, K. D., & Yaqoob, T. 2009, *MNRAS*, 397, 1549
 Noguchi, K., Terashima, Y., Ishino, Y., et al. 2010, *ApJ*, 711, 144
 Nousek, J. A., & Shue, D. R. 1989, *ApJ*, 342, 1207
 Parker, M. L., Marinucci, A., Brenneman, L., et al. 2014, *MNRAS*, 437, 721
 Puccetti, S., Comastri, A., Fiore, F., et al. 2014, *ApJ*, 793, 26
 Reynolds, C. S. 1999, in *ASP Conf. Ser. 161, High Energy Processes in Accreting Black Holes*, ed. J. Poutanen, & R. Svensson (San Francisco, CA: ASP), 178
 Ricci, C., Ueda, Y., Koss, M. J., et al. 2015, *ApJL*, 815, L13
 Rigby, J. R., Diamond-Stanic, A. M., & Aniano, G. 2009, *ApJ*, 700, 1878
 Risaliti, G., Gilli, R., Maiolino, R., & Salvati, M. 2000, *A&A*, 357, 13

- Roy, A. L., Ulvestad, J. S., Wilson, A. S., et al. 2000, in *Perspectives on Radio Astronomy: Science with Large Antenna Arrays*, ed. M. P. van Haarlem (ASTRON), 173
- Salvati, M., Bassani, L., della Ceca, R., et al. 1997, *A&A*, 323, L1
- Sanders, D. B., Soifer, B. T., Elias, J. H., Neugebauer, G., & Matthews, K. 1988, *ApJL*, 328, L35
- Schawinski, K., Koss, M., Berney, S., & Sartori, L. F. 2015, *MNRAS*, 451, 2517
- Smith, R. K., Brickhouse, N. S., Liedahl, D. A., & Raymond, J. C. 2001, *ApJL*, 556, L91
- Stern, D. 2015, *ApJ*, 807, 129
- Stern, D., Assef, R. J., Benford, D. J., et al. 2012, *ApJ*, 753, 30
- Stern, D., Djorgovski, S. G., Perley, R. A., de Carvalho, R. R., & Wall, J. V. 2000, *AJ*, 119, 1526
- Stern, D., Eisenhardt, P., Gorjian, V., et al. 2005, *ApJ*, 631, 163
- Treister, E., Natarajan, P., Sanders, D. B., et al. 2010, *Sci*, 328, 600
- Treister, E., & Urry, C. M. 2005, *ApJ*, 630, 115
- Treister, E., Urry, C. M., Chatzichristou, E., et al. 2004, *ApJ*, 616, 123
- Treister, E., Urry, C. M., & Virani, S. 2009, *ApJ*, 696, 110
- Tueller, J., Mushotzky, R. F., Barthelmy, S., et al. 2008, *ApJ*, 681, 113
- Ueda, Y., Akiyama, M., Hasinger, G., Miyaji, T., & Watson, M. G. 2014, *ApJ*, 786, 104
- Ueda, Y., Eguchi, S., Terashima, Y., et al. 2007, *ApJL*, 664, L79
- Van Wassenhove, S., Volonteri, M., Mayer, L., et al. 2012, *ApJL*, 748, L7
- Vasudevan, R. V., Brandt, W. N., Mushotzky, R. F., et al. 2013, *ApJ*, 763, 111
- Vasudevan, R. V., & Fabian, A. C. 2009, *MNRAS*, 392, 1124
- Veilleux, S., & Osterbrock, D. E. 1987, *ApJS*, 63, 295
- Wachter, K., Leach, R., & Kellogg, E. 1979, *ApJ*, 230, 274
- Wik, D. R., Hornstrup, A., Molendi, S., et al. 2014, *ApJ*, 792, 48
- Winter, L. M., Mushotzky, R. F., Reynolds, C. S., & Tueller, J. 2009, *ApJ*, 690, 1322
- Worsley, M. A., Fabian, A. C., Bauer, F. E., et al. 2005, *MNRAS*, 357, 1281
- Xue, Y. Q., Wang, S. X., Brandt, W. N., et al. 2012, *ApJ*, 758, 129